Icarus 332 (2019) 92–110

Contents lists available at ScienceDirect

Icarus

journal homepage: www.elsevier.com/locate/icarus

Formation of sinuous ridges by inversion of river-channel belts in Utah, USA, with implications for Mars

Alistair T. Hayden[a,*], Michael P. Lamb[a], Woodward W. Fischer[a], Ryan C. Ewing[b], Brandon J. McElroy[c], Rebecca M.E. Williams[d]

[a] Division of Geological and Planetary Sciences, California Institute of Technology, 1200 E California Blvd, Pasadena, CA 91125, USA
[b] Department of Geology and Geophysics, Texas A&M University, 3115 TAMU, College Station, TX 77843, USA
[c] Department of Geology and Geophysics, University of Wyoming, 1000 E University Avenue, Laramie, WY 82071, USA
[d] Planetary Science Institute, 1700 East Fort Lowell Rd., Suite 106, Tucson, AZ 85179, USA

ARTICLE INFO

Keywords:
Mars, surface
Mars
Earth
Geological processes

ABSTRACT

Sinuous ridges are important landforms on the surface of Mars that show promise for quantifying ancient martian surface hydrology. Morphological similarity of these ridges to river channels in planform led to a hypothesis that ridges are topographically inverted river channels, or "inverted channels", formed due to an erosion-resistant channel-filling material that preserved a snapshot of the channel geometry in inverted relief due to differential erosion. An alternative deposit-inversion hypothesis proposes that ridges represent exhumed river-channel belts, with geometries that reflect the lateral migration and vertical aggradation of rivers over significant geologic time, rather than the original channel geometry. To investigate these hypotheses we studied sinuous ridges within the Cretaceous Cedar Mountain Formation near Green River, Utah, USA. Ridges in Utah extend for hundreds of meters, are up to 120 m wide, and stand up to 39 m above the surrounding plain. Ridges are capped by sandstone bodies 3–10 m thick that contain dune- and bar-scale inclined stratification, which we interpret as eroded remnants of channel belts that record the migration and aggradation of single-thread, sand-bedded rivers, rather than channel fills that can preserve the original channel geometry. Caprocks overlie mudstones and thinner sandstone beds that are interpreted as floodplain deposits, and in cases additional channel-belt sandstones are present lower in the ridge stratigraphy. Apparent networks from branching ridges typically represent discrete sandstone bodies that cross at different stratigraphic levels rather than a coeval river network. Ridge-forming sandstone bodies also have been narrowed during exhumation by cliff retreat and bisected by fluvial erosion. Using a large compilation of channel-belt geometries on Earth and our measurements of ridges in Utah, we propose that caprock thickness is the most reliable indicator of paleo-channel geometry, and can be used to reconstruct river depth and discharge. In contrast, channel lateral migration and caprock erosion during exhumation make ridge breadth an uncertain proxy for channel width. An example in Aeolis Dorsa, Mars, illustrates that river discharge estimates based solely on caprock width may differ significantly from estimates based on caprock thickness. Overall, our study suggests that sinuous ridges are not inverted channel fills, but rather reflect exhumation of a thick stratigraphic package of stacked channel belts and overbank deposits formed from depositional rivers over significant geologic time.

1. Introduction

Sinuous topographic ridges are abundant landforms on the surface of Mars, and they are important for reconstructing the history of surface water on early Mars (e.g.; Williams, 2007; Burr et al., 2010; Moore et al., 2003; Palucis et al., 2014; Fassett and Head, 2005; Kite et al., 2015a, 2015b; Cardenas et al., 2017; Goudge et al., 2018; Fig. 1A–B). Some sinuous ridges have been interpreted to be igneous wrinkle ridges, glacial moraines, eskers, or exhumed igneous and sedimentary dikes (Kargel and Strom, 1992), but the most common interpretation is they reflect—in some fashion—topographically inverted river channels, owing to their similarity to river channels in planform (Pain and Ollier, 1995; Pain et al., 2007) (Fig. 1). The inverted-channel hypothesis suggests that river channels were filled with a more resistant material, such as a lava flow (e.g., Stanislaus Table Mountain described in Burr et al., 2010), or a coarse or well-cemented sediment (e.g., Maizels,

* Corresponding author.
E-mail address: ahayden@caltech.edu (A.T. Hayden).

https://doi.org/10.1016/j.icarus.2019.04.019
Received 31 August 2018; Received in revised form 15 February 2019; Accepted 18 April 2019
Available online 22 April 2019
0019-1035/ © 2019 Elsevier Inc. All rights reserved.

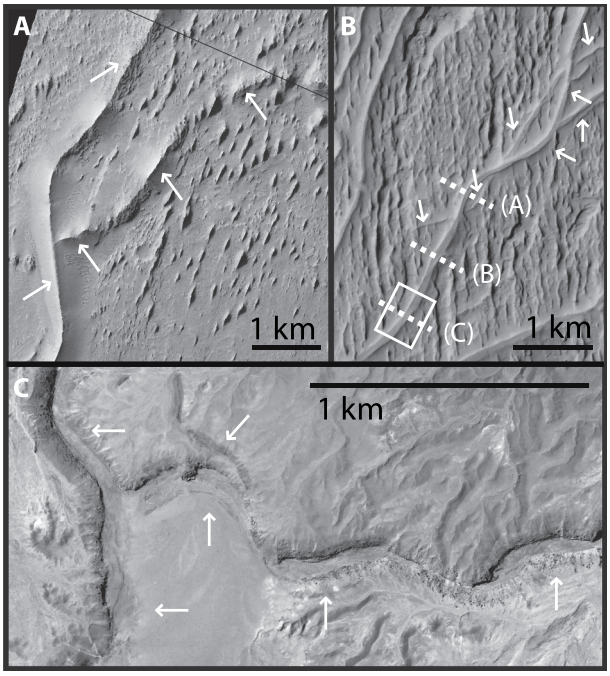

Fig. 1. Examples of sinuous ridges from Mars and Earth. Arrows point to ridges. A) Long ridge with a single branch in Aeolis Dorsa, Mars. Small parallel bumps are yardangs (Coordinates −4.67, 151.13; HiRISE image PSP_010533_1755; credit: NASA/JPL/University of Arizona). B) At least two sets of stratigraphically distinct ridges on Mars with superposed yardangs. This is part of a larger ridge network that has been interpreted both as convergent flow to the lower left based on channel inversion and divergent flow to the upper right on the basis of deposit inversion (Lefort et al., 2012, 2015; DiBiase et al., 2013). White box indicates section shown in Fig. 15A, dotted lines denote cross section locations in Fig. 15B. (Coordinates −6.105, 151.479; Aeolis Dorsa, Mars; CTX image B18_016691_1740_XN_06S208W; credit: NASA/JPL/Malin Space Science Systems). C) Branching, segmented ridges in our field area, south of Green River, Utah (38.876, −110.271; National Agriculture Image Program 2014 image).

1987, 1990), and that subsequent deflation of the neighboring land left the channel fill as a topographic high (Fig. 2A). Because of their putative connection to river processes, sinuous ridges on Mars have been used to infer paleo-hydrology (Fassett and Head, 2005; Burr et al., 2010; Irwin et al., 2015), global history of water (Kite et al., 2015a, 2015b), tectonics (Lefort et al., 2015), and large oceans or seas (DiBiase et al., 2013; Cardenas et al., 2017). In addition to being detectable and measurable from orbital data, they also are valuable to rover missions due to their presence in Gale Crater, the site of the Mars Science Laboratory rover (Anderson and Bell, 2010; Le Deit et al., 2013; Palucis et al., 2014), and in several sites of interest for future missions (e.g., Eberswalde crater (Irwin et al., 2015), Holden crater (Grant and Wilson, 2012), Jezero Crater (Goudge et al., 2018), Mawrth Valles (Loizeau et al., 2015), Melas Chasma (Williams and Weitz, 2014), and Aram Dorsum (Balme et al., 2016)).

Although the inverted-channel hypothesis is commonly assumed on Mars, little work has been done to evaluate it. Part of the issue is that outcrop-scale observations are needed to confirm the nature of the ridge material and whether the ridges represent true casts of channels, and these observations are not readily available on Mars. Many studies assume that ridge geometries, such as width and planform curvature, closely approximate the corresponding river channel geometries (Fig. 2A), and use these parameters in empirical formulas developed from terrestrial meandering rivers to calculate river discharge (e.g., Burr et al., 2010; Williams et al., 2013; Palucis et al., 2014; Kite et al., 2015b). However, another possibility is that the sinuous ridges represent exhumed river-channel belts (Figs. 2B, 3) (DiBiase et al., 2013;

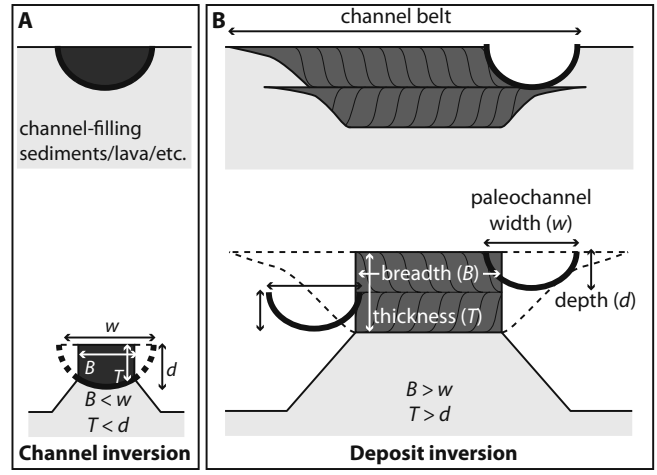

Fig. 2. Schematic hypotheses for the formation of fluvial sinuous ridges. A) Schematic of the topographic-inversion hypothesis: a channel (black semi-circle) has been filled with a resistant material (dark gray) and is subsequently exhumed to form a ridge with caprock dimensions (breadth, *B*, and thickness, *T*) that are slightly smaller than the original channel dimensions (width, *w*, depth, *d*) due to erosion. B) Schematic of the deposit-inversion hypothesis: a channel (black semi-circle) aggrades and migrates across the floodplain (light gray) building a channel-belt sandstone body (medium gray) that is larger than the original channel. During exhumation, erosion modifies the channel-belt sandstone primarily by lateral backwasting reducing the ridge breadth. The channel fill may not be preserved in the caprock sandstone, as indicated.

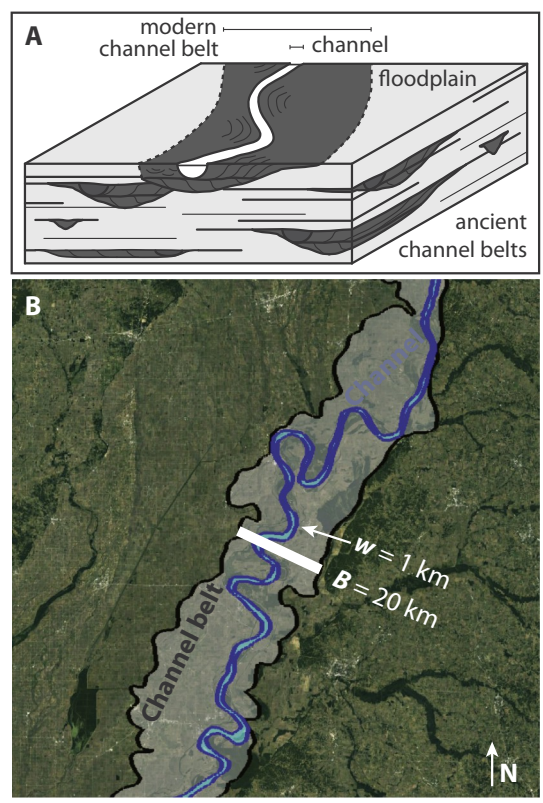

Fig. 3. A) Stratigraphic architecture of a fluvial depositional basin including a sinuous single-thread river channel (white), floodplain deposits (light gray), multiple generations of stacked channel belts (medium gray), and rare channel fills (dark gray). Note that channel belts have widths, thicknesses, and sinuosities that can be different than the geometry of the channel. B) Example of a modern channel belt: Mississippi River below Cairo, IL. Channel belt outline is from Fernandes et al. (2016). Landsat true color image, December, 2016. Channel belt width, *B*, is much larger than the channel width, *w*.

Matsubara et al., 2015; Kite et al., 2015a; Irwin et al., 2015), which DiBiase et al. (2013) termed deposit inversion. For instance, it is well known that the stratigraphic architecture of depositional fluvial systems typically shows discrete tabular bodies of sandstone or conglomerate that are interspersed within a finer grained mudstone floodplain facies (e.g., Friend et al., 1979; Gibling, 2006; Heller and Paola, 1996), which could lead to differential erosion and exhumation of the coarser bodies (Fig. 3A). Fluvial sandstone and conglomerate bodies are typically far wider and thicker than the original river channels because the bodies formed from lateral migration, aggradation, and abandonment and reoccupation of the river channel within its channel belt (e.g., Mohrig et al., 2000; Fig. 3). The bend wavelength for an entire channel belt also is typically different than the bend wavelength of the channel (Fig. 3), which can be observed in examples for both modern and ancient systems (e.g., Fernandes et al., 2016; Martin et al., 2018). On Mars, supporting observations for deposit inversion includes ridges at distinct stratigraphic levels and ridges comprised of amalgamated channel deposits (Malin and Edgett, 2003; Moore et al., 2003; Burr et al., 2009, 2010; DiBiase et al., 2013; Kite et al., 2013, 2015a, 2015b; Cardenas et al., 2017).

In contrast to channel belts, deposits that fill and preserve the geometry of a paleo-channel (i.e., channel fills) are comparatively rare, and where they do exist are typically amalgamated within a larger channel-belt deposit (Ielpi and Ghinassi, 2014; Durkin et al., 2017 (Fig. 3A)). Channel fills also are commonly finer-grained overbank deposits (e.g., Bridge, 2003; Reijenstein et al., 2011; Musial et al., 2012; Bhattacharya et al., 2016), similar to the floodplain deposits that are eroded during ridge formation, and so may be less likely to be preserved as resistant ridges. While some workers on Mars have recognized, and in cases avoided analysis on, ridges with signs of lateral channel migration by bend growth or ridges with variable breadths that may indicate significant erosion (e.g., Burr et al., 2010), the assumption that ridge geometries closely approximate the original channel geometries is pervasive (Moore et al., 2003; Jerolmack et al., 2004; Fassett and Head, 2005; Burr et al., 2010; Williams et al., 2013; Palucis et al., 2014; Kite et al., 2015b). For instance, ridges with breadth-to-bend wavelength ratios that are similar to meandering rivers on Earth is commonly used to support the hypothesis that ridge geometries closely match the original channel geometries (e.g., Burr et al., 2010; Kite et al., 2015b).

Distinguishing between channel inversion and deposit inversion is important. Unlike the inverted channel model (Fig. 2A), the deposit inversion hypothesis of DiBiase et al. (2013) implies that sinuous ridges are not snapshots in time of a single geomorphic surface, but rather they are an amalgamation of fluvial deposits that represent a rich record of long-lived fluvial activity (Fig. 2B). The two models can also indicate opposite paleo-flow directions. For example, the modern topographic slope of branching ridge networks in Aeolis Dorsa, Mars (Fig. 1B) suggests a convergent drainage of river channels typical of uplands (Lefort et al., 2012), whereas analysis of the deposit stratigraphy implies a divergent, depositional channel network with the opposite flow direction (DiBiase et al., 2013; Lefort et al., 2015).

A better understanding of the processes that formed sinuous ridges can arise from focused studies on Earth where both ridge morphology and outcrop sedimentology are readily observable. Most previous studies of terrestrial sinuous ridges have focused on fluvial sedimentology, due to the excellent outcrop exposure, with little attention paid to ridge formation (e.g., Stokes, 1961; Derr, 1974; Harris, 1980; Friend et al., 1979; Friend, 1989; Maizels, 1987, 1990; Mohrig et al., 2000; Cuevas Martínez et al., 2010; Nuse, 2015). Some recent work has addressed these landforms as analogs for Mars (Pain et al., 2007; Williams et al., 2007; DiBiase et al., 2013; Zaki et al., 2018) including the role of cementation in forming the ridges (Clarke and Stoker, 2011; Williams et al., 2011). Although they did not seek to directly test the deposit and channel inversion models, Williams et al. (2009), working on ridges of the Cedar Mountain Formation in Utah, showed discrepancies between paleo-hydraulic reconstruction techniques that utilize ridge morphology versus deposit sedimentology, and cautioned against some of the common assumptions made in the channel inversion hypothesis on Mars.

Herein, we built on the analysis of Williams et al. (2007, 2009, 2011) of sinuous ridges in the Cretaceous-age Cedar Mountain Formation of southeastern Utah, and provided new observations and analyses to test the channel- and deposit-inversion hypotheses. In addition, we generated a global compilation of channel-belt dimensions on Earth, which we used to develop a method for reconstructing river discharge from exhumed channel belts. After describing the terminology and study sites in Sections 2 and 3, field and remote-sensing methods are discussed in Section 4, and the paleo-hydraulic reconstruction method for channel belts is proposed in Section 5. Section 6 presents results for ridge and ridge-network geometries, outcrop sedimentology, and stratigraphy in Utah. Finally, we evaluate the channel- and deposit-inversion hypotheses in Section 7, and discuss implications for reconstructing paleo-hydraulics and depositional environments from sinuous ridges on Mars.

2. Terminology

Terminology related to ridges, channels, and river deposits is often unclear or conflicting in previous studies. Here we use the term channel to reflect the topographic trough that is a conduit for river water flow (Fig. 3A). Channel fills are deposits that fill an abandoned channel following cutoff or avulsion (e.g., Bridge, 2003; Gibling, 2006; Blum et al., 2013) (Fig. 3A). Channel fills are important where preserved because they record the original shape of the channel; i.e., the channel-fill container is the original channel (Reijenstein et al., 2011; Musial et al., 2012; Bhattacharya et al., 2016). However, the channel-filling material is typically not transported within the active channel, but rather tends to be fine-grained overbank deposits that drape channels after they are abandoned by the main flow. Overbank deposits are from unchannelized flood flows that spill out of the active channel onto the floodplain. The fill material can also be lava (e.g., Stanislaus Table Mountain described in Burr et al., 2010) or eolian sediments, for example, that fill an abandoned channel.

Deposits from sediment transported within the active channel are referred to as channel deposits, which can be laterally extensive and thick as a result of lateral migration and aggradation of the channel (Fig. 3A). Channel deposits in sand-bedded rivers are often organized into channel bars and dunes, which make distinct scales of inclined stratification that relate to the depth of the channel. An amalgamation of channel deposits is referred to as a channel belt (also known as a channel-belt sand body, channel sandstone body, channel body, or channel complex in previous work; Fig. 3) (e.g., Gibling, 2006; DiBiase et al., 2013; Blum et al., 2013). A channel belt is often thicker and wider than the paleo-channel due to lateral channel migration, aggradation, and avulsion and reoccupation that can juxtapose and/or amalgamate multiple generations of channel deposits. Thus, channel belts can contain stratigraphic packages that record single or multiple generations of channel lateral migration (or “storeys”) (Mackey and Bridge, 1995). Channel belts, therefore, are distinct from channel fills in their formation process, geometry, and sedimentology. The stratigraphic architecture of fluvial depositional basins is typically dominated by stacked channel-belt sand bodies and floodplain deposits, not channel fills (Heller and Paola, 1996).

We use the term inverted channel to refer to a channel fill that stands as a topographic high (ridge) because of preferential deflation of the surrounding terrain. Hence, inverted channel by our definition implicitly assumes topographic inversion of a channel fill, and this is also how the term is often used on Mars (e.g., Burr et al., 2010). When the ridge formation process is unknown, we favor a non-interpretive landform descriptor like sinuous ridge. Ridges formed from exhumed channel belts, in contrast, are composed of channel deposits and should have geometries that are unlike the original channel due to river lateral

migration and aggradation (e.g., Robinson and McCabe, 1997; Jerolmack and Mohrig, 2007; Blum et al., 2013). Previous workers on both Earth and Mars commonly used the terms paleo-channel or inverted channel to describe ridges, but their intention to implicate channel fills versus channel belts was not always explicit (e.g., Derr, 1974; Harris, 1980; Maizels, 1987; Burr et al., 2010; Palucis et al., 2014; Kite et al., 2015a, b; Jacobsen and Burr, 2018; Fig. 2A). Nonetheless, many studies used ridge width or ridge curvature as direct proxies for the original channel width or channel curvature (Derr, 1974; Harris, 1980; Burr et al., 2010; DiBiase et al., 2013; Williams et al., 2013; Palucis et al., 2014; Kite et al., 2015b), and so implicitly inferred topographic inversion of a channel fill, or a channel-belt that coincidently has geometries similar to the original channel. We investigated whether ridges in Utah are exhumed channel fills (inverted channels), or rather exhumed channel belts (Fig. 2).

3. Study site and previous work

We studied fluvial sinuous ridges near the town of Green River, Utah, referred to herein as the Green River site, that are often used as terrestrial analogs to sinuous ridges on Mars (Williams et al., 2007, 2009, 2011; Burr et al., 2010; Jacobsen and Burr, 2017) (Fig. 4). The ridges are composed of sedimentary rocks from the early Cretaceous Ruby Ranch member of Cedar Mountain Formation in Utah, near the San Rafael Swell, a monocline, and are mostly flat lying with local stratal dips less than ~5° (Bates, 1952; Sable, 1958; Witkind, 1988; Doelling et al., 2015). The Ruby Ranch Member is characterized by drably variegated mudstones with interspersed sandstone bodies that form sinuous ridges (Kirkland et al., 1997, 1999). Accommodation space was generated in a foreland basin during thrusting associated with the eastward-migrating Sevier Orogeny (DeCelles and Currie, 1996; Currie, 2002; DeCelles and Coogan, 2006). The Sevier Mountains and Mogollon Highlands confined the Cedar Mountain Formation to the west and south. Detrital zircon provenance (Ludvigson et al., 2015) indicates sediment sources from these highlands, which is consistent with flow directions toward the north (e.g., Harris, 1980; Nuse, 2015). The Cedar Mountain Formation was deposited over 30 M.y. (Kirkland et al., 1997), and best age constraints for the inverted-channel-rich Ruby Ranch Member bracket it with tephra to between

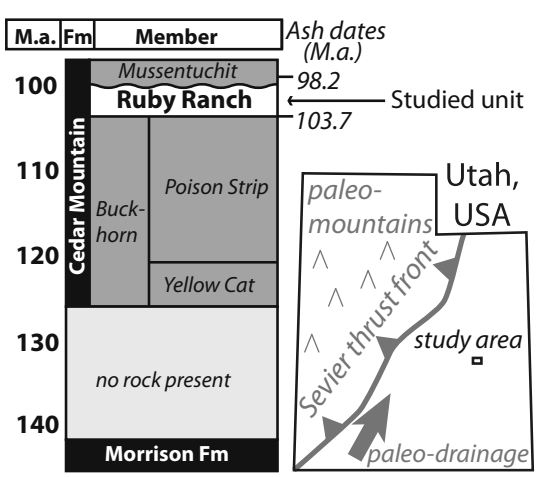

Fig. 4. Representative stratigraphy, paleogeography, and modern geography of the field area. Left) representative stratigraphic section of Ruby Ranch member (after Kirkland et al., 1997; with revised dates from Ludvigson et al., 2015; Garrison et al., 2007). The Ruby Ranch member deposition duration is constrained by ash dates from the basal contact with the Buckhorn conglomerate (Garrison et al., 2007) and a bed within the Mussentuchit (Ludvigson et al., 2015) that unconformably overlies the Ruby Ranch Member, to within 5.5 M.y. Right) Interpreted paleogeography of the study area (after Ludvigson et al., 2015).

103.7 ± 2.6 M.a. (Ludvigson et al., 2015) and 98.2 ± 0.6 M.a. (Garrison et al., 2007) (Fig. 4).

The ridges of the Cedar Mountain Formation have been noted since Stokes (1944), but were first studied in detail by Harris (1980) at the Green River site. He mapped bar and dune migration directions, and noted that bar migration directions were often oblique to the ridge margins, and therefore inferred these were point bars associated with river meandering. He also assumed that several ridges that align in orientation in map view are segments of a sandstone body from a single river system that has been dissected by erosion. Although Harris recognized the ridge-capping sandstones as composed of amalgamated channel deposits that have been eroded, he nonetheless used the caprock dimensions as a proxy for the paleo-channel dimensions, and calculated annual-flood discharges of 215–600 m^3/s using an empirical relation between river discharge and channel width and depth from Schumm (1972).

Williams et al. (2009) used similar approaches at the Green River site to reconstruct discharge from empirical relations for single-thread rivers between discharge and channel width, and for meandering rivers between discharge and bend wavelength and bend radius of curvature (Schumm, 1972; Williams, 1984, 1988; Osterkamp and Hedman, 1982). However, recognizing the complicating effects of channel migration and caprock erosion, Williams et al. (2009) proposed that the third quartile of the maximum measured ridge width is a good proxy for channel width. They also compared the discharge reconstruction using ridge width to the discharge required to move sediment, a necessary lower limit, and found significant differences between the different methods. Williams et al. (2009) recognized that the ridges occur at distinct stratigraphic levels, and so the ridges must be deposits from rivers that existed at different time periods.

Given the present uncertainty as to whether channel- or deposit-inversion hypotheses apply, we revisited the classic Green River site to explicitly test the hypotheses and explore their implications for Mars. Our approach was to use process-based sedimentology to reconstruct the channel dimensions and paleo-hydraulics in way that was independent of ridge geometry. We then compared the results from ground-based observations (sedimentology and stratigraphic sections) to those based only on ridge geometry (knowable from remote sensing data) to evaluate the channel-inversion and deposit-inversion hypotheses.

4. Methods

We identified ridge segments and mapped their planform relationships using NAIP air photos (1 m resolution) and digital elevation models (DEM; 5 m resolution) acquired from the Utah Geologic Survey (Fig. 5A). We also surveyed each ridge with an unmanned aerial vehicle (UAV) and generated ortho-photos and DEMs at < 20 cm per pixel using the photogrammetry software Agisoft PhotoScan. To compare the relative stratigraphic position of ridges, we needed to account for tectonic tilting associated with the San Rafael Swell. We used local measurements as reported on U.S. Geological Survey maps (Sable, 1958; Doelling et al., 2015) of bedding dips and dip directions 1° to the 000° for this area, and then subtracted this plane from the coarse DEM to create an elevation model with tectonic tilt removed (Fig. 5). We verified the correction by tracing in airphotos the top of a prominent mudstone bed in a nearby cliff, discretizing the points in the DEM, and fitting a plane using least-squares regression to the contact elevation points, which yielded a dip of 1.4° to 014°. These corrections were similar to those reported by Williams et al. (2009) [1.5°–1.9° to the NE], who similarly used a nearby mudstone bed in the underlying Morrison Formation as a datum.

Similar to previous work (e.g., Harris, 1980; Williams et al., 2009), we initially treated each ridge segment as distinct, then used field observations of paleo-flow indicators and stratigraphic position to discuss which ridges represent the same stratigraphic intervals and which are

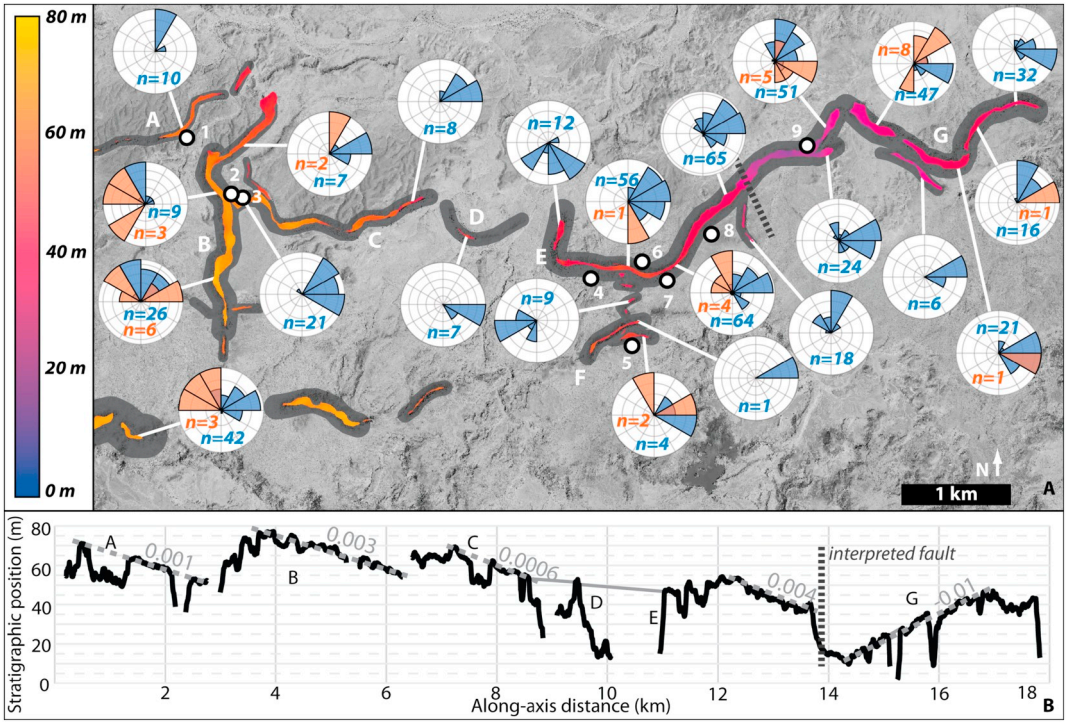

Fig. 5. Sinuous ridges in the field area (center of map is 38.871, −110.230). A) Map showing caprocks colored by their stratigraphic position (elevation corrected for tectonic tilt; see Section 4) and talus-covered flanks of the ridges highlighted in gray. Ridge names are given in capital letters, stratigraphic sections (see Fig. 6) are given by numbers. Rose diagrams show accretion directions of dune sets (blue) and bar strata (red) binned by caprock segment. B) Caprock centerline position in stratigraphic space (elevation corrected for tectonic tilt; see Section 4) versus distance along a ridge centerline, with linear-least-squares-fits to caprock top surfaces (interpreted to be minimally eroded; see Section 7.2) given in dotted gray lines. A fault is located at the position indicated (Sable, 1958); note offset of the ridgetop. Letters correspond to ridge labels in panel A. (For interpretation of the references to color in this figure legend, the reader is referred to the web version of this article.)

distinct. Note that our names for each ridge segment differ from previous work (Harris, 1980; Williams et al., 2009) because our focus differed from theirs. We paid special attention to ridges that appear to cross in planview, forming an 'X' pattern, or branch forming a 'Y' pattern to evaluate if they represent bifurcating paleo-channels or the intersection of channel deposits at different stratigraphic levels. Ridge centerlines were manually traced on air photos, and we discretized the centerlines into a series of nodes with a spacing approximately equivalent to the average top width of the caprock (i.e., 100 m). Subsequent measurements of breadth and relief were made at each node, and the average and 5th–95th percentile range is reported for each ridge segment (Table S1). Measurements of caprock breadth (B), defined as the caprock top width perpendicular to the local ridge centerline trace, were made using the ortho-rectified air photos.

Measurements of ridge shape and relief were made from the Utah Geologic Survey DEMs (5 m/pixel). Ridge relief was calculated from the DEM as the difference between the average elevation of the top of the caprock with the elevation of the inflection point in the ridge transect, where it transitions to a flat plane. Average along-axis ridge slope was measured for each ridge by taking the best-fit linear regression to the ridge-centerline elevation profile on the caprock, with the tectonic tilt removed (Fig. 5B), and the 5th–95th percentile confidence interval was recorded.

For each ridge, we measured vertical stratigraphic sections in the field, and noted bedding types (Fig. 6). Ridges are composed of a flat-topped, relatively thick, cliff-forming sandstone or conglomerate unit on top, referred to as the caprock, that is typically atop a talus-covered slope composed of mudstone and thinner sandstone bodies. Caprock thickness, T, was measured as the vertical thickness of the uppermost sandstone body in each stratigraphic section (e.g., Fig. 6). We traced beds laterally along a ridge to correlate stratigraphic position for measured sections on the same ridge. For sandstone and conglomerate, we documented the median grain size (D_{50}) by eye with a grain size card and cross-bedding set thicknesses with a ruler. Dip directions of ripple and dune cross-sets were measured using cross section exposures (Figs. 7B–D), as well as plan-view exposures of bedform troughs, such as rib-and-furrow structures (Fig. 7C; Stokes, 1953; Miall, 1996; Bhattacharya et al., 2016; Wu et al., 2016). Most ridge caprocks have an additional, larger (> ~0.5 m) scale of cross stratification, which lacks troughs and rolls over and pinches out laterally, which we interpreted to represent bar clinoforms or channel-margin lateral accretion bedding (Fig. 7F; e.g., Miall, 1996; Mohrig et al., 2000; Hajek and Heller, 2012; Blum et al., 2013; Bhattacharya et al., 2016).

5. Paleo-hydraulic reconstruction calculations

5.1. Inverted channels

Based on the channel topographic inversion hypothesis, the bankfull channel width, w, bankfull depth, d and channel bed slope, S, are assumed to be accurately reflected as the ridge breadth, caprock thickness, and caprock top slope. From conservation of mass:

$$Q = Udw \tag{1}$$

where U is the cross-section-average bankfull flow velocity and Q is the bankfull channel discharge.

We determined flow velocity from the flow resistance method of Engelund and Hansen (1967) that is based on the idea of partitioning hydraulic roughness in sand-bedded rivers between the bed sediment (skin friction) and drag from bedforms such as ripples and dunes (Einstein, 1950). Note that this relation is intended only to apply to sand-bedded rivers with dunes, such as occur in the study area; for gravel-bedded rivers, we recommend using the friction relation of

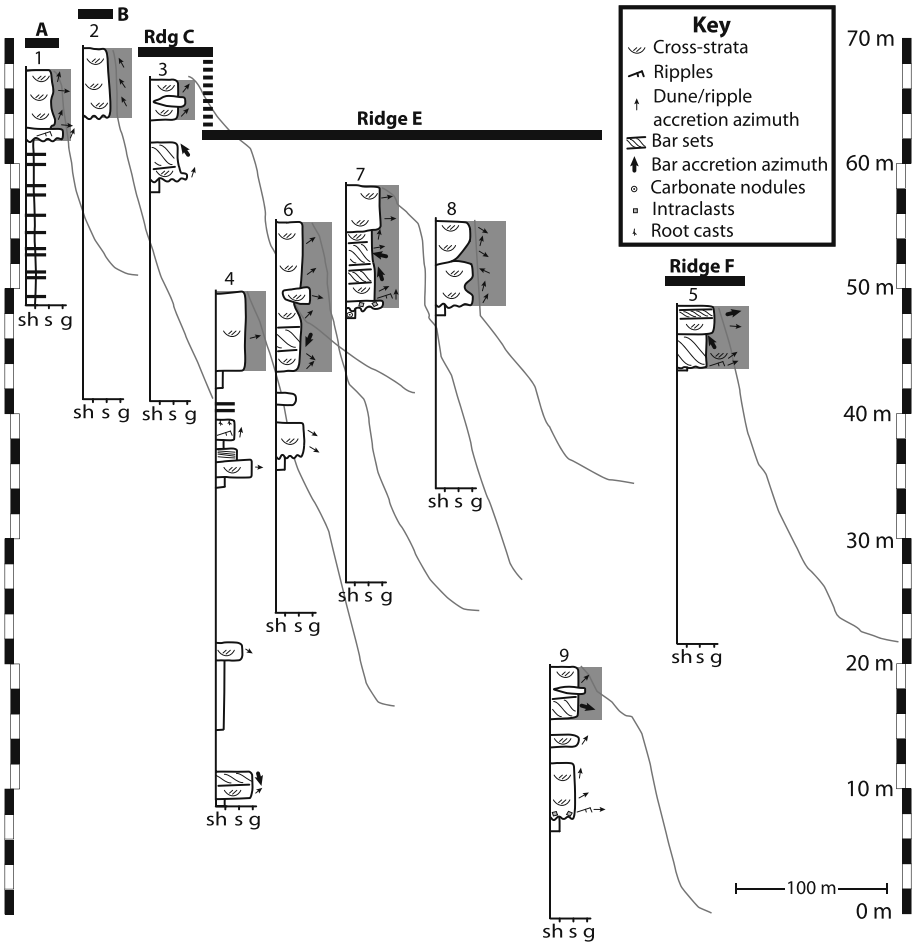

Fig. 6. Representative stratigraphic sections placed in stratigraphic position along ridges. Bedform accretion directions noted by arrow azimuth, and median grain size given by edge of each section (sh – shale, s – medium sand sandstone, g – granule conglomerate). Positions of the stratigraphic sections are referenced to the digital elevation model with the tectonic tilt removed. Section 9 is offset by a fault (see Fig. 5), resulting in its lower position. Gray line curving off the right shoulder of the stratigraphic section represents the topographic profile from caprock down to ridge bottom, extracted from the 0.5-meter-per-pixel photogrammetric digital elevation model, and exaggerated 10× vertically to fit (see Fig. 15B for better detail). The caprock is highlighted with a gray box, and is often visible in the topographic profiles as a break in the slope. Most ridges are covered with talus below the caprock; covered sections are blank on the stratigraphic sections.

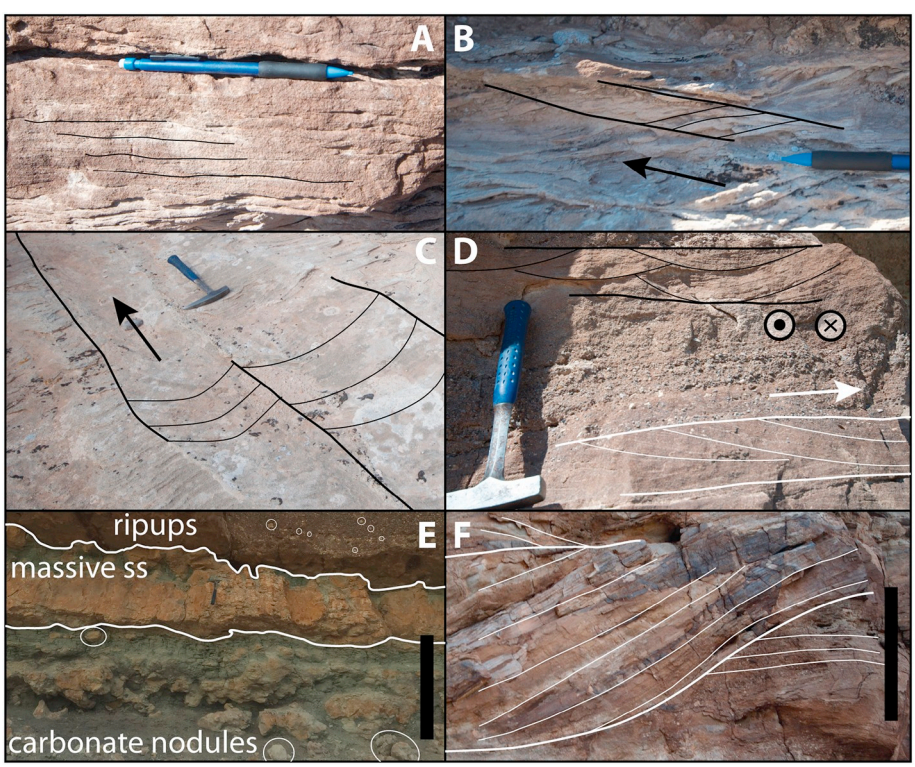

Fig. 7. Sedimentary structures observed in the ridges: A) planar-laminated fine sandstone; B) climbing ripples, paleo-flow along arrow; C) rib-and-furrow structures seen in planview from dune trough cross stratification, with sets indicated by thin lines and bounded by thick lines, paleo-flow along arrow; D) trough cross-stratification seen in cuts both perpendicular (black lines, indicating trough cross-stratification) and parallel (white lines), with sets defined by thin lines and set boundaries indicated by thick lines; E) mud intraclasts circled within sandstone, massive sandstone, carbonate-nodule-rich mudstone; F) bar-scale accretion sets (thick lines indicate set boundaries, thin lines indicate inclined bedding) showing rollover to the top right, indicating that close to the full bar height is preserved. Pencil in A and B is approximately 0.2 m, hammer in C and D is approximately 0.3 m, scale bars in E and F are approximately 1 m.

Ferguson (2007). Following the method of Engelund and Hansen (1967), the skin friction component of the Shields stress, τ_s^*, was calculated from

$$\tau_s^* = 0.06 + 0.4\tau^{*2} \quad (2)$$

where τ^* is the dimensionless bankfull Shields stress, and τ_s^* in Eq. (2) should not exceed τ^*. The bankfull Shields stress, under the assumption of steady and uniform flow, is

$$\tau^* = dS/RD_{50} \quad (3)$$

where $R = (\rho_s - \rho_w) / \rho_w$, ρ_w is water density, ρ_s is the density of sediment, and D_{50} is the median particle diameter. The skin friction component of the Shields stress is defined as

$$\tau_s^* = u_s^{*2}/RgD_{50} \quad (4)$$

where g is acceleration due to gravity. The skin friction component of the shear velocity (u_s^*) is related to the flow velocity through (Engelund and Hansen, 1967)

$$U/u_s^* = (1/\kappa)\ln[11d_s/k_s] \quad (5)$$

where $\kappa = 0.4$ is von Karman's constant, $k_s = 2.5D_{50}$ is the grain roughness lengthscale and d_s is the skin friction component of the flow depth under steady and uniform flow ($u_s^* = (gd_sS)^{0.5}$).

To apply the Engelund and Hansen method, we combined Eqs. (4)–(5) and rearranged to solve for flow velocity as

$$U = (1/\kappa)\ln[11(RD_{50}/Sk_s)\,\tau_s^*]\,(RgD_{50}\,\tau_s^*)^{0.5} \quad (6)$$

in which we set $R = 1.65$ and $g = 9.81$ m/s^2. To find the bankfull discharge under the channel inversion assumption, Eq. (6) is combined with Eq. (1); grain size, D_{50}, is constrained by field data; d, w and S are inferred from the ridge caprock geometry as discussed in Section 4; and τ_s^* comes from Eqs. (2)–(3). We propagated uncertainty from the measured breadth along a given ridge, using the 5% and 95% bounds on the ridge breadth distribution, through the discharge calculation (Eqs. (1)–(6)) using standard Gaussian error propagation.

Note that Eqs. (1)–(6) can be combined and rewritten as a simple power-law relation between discharge and channel width, which is similar to those often used on Earth (Maizels, 1987; Williams et al., 2009) and other extraterrestrial bodies (Jaumann et al., 2008; Burr et al., 2010; Matsubara et al., 2015; Irwin et al., 2015; Jacobsen and Burr, 2018),

$$Q = a\,w^b \quad (7)$$

where $a = (gS)^{1/2}C_f^{-1/2}(w/d)^{-3/2}$ and $C_f = gdS/U^2$, which depends on D_{50}, d, and S (Eq. (6)). To demonstrate the comparison, we inserted values common to single-threaded sand-bedded rivers ($g = 9.81$ m/s^2, $S = 0.005$, $C_f = 0.02$, $w/d = 18$) and found $a = 0.02$ and $b = 2.5$, which are similar to empirical values (e.g., $a = 0.1$ and $b = 1.86$ from Eaton (2013); $a = 1.9$ and $b = 1.22$ from Osterkamp and Hedman (1982)) that are often used on extraterrestrial bodies (Jaumann et al., 2008; Burr et al., 2010; Matsubara et al., 2015; Jacobsen and Burr, 2018). Although using empirical fits to find a and b in Eq. (7) is simpler, we prefer using Eqs. (1)–(6) because they explicitly incorporate gravity and sediment and fluid properties that can vary in different environments, and allow for variable C_f due to the presence of dunes. We therefore only use Eq. (7) to demonstrate the difference between these approaches.

The biggest uncertainty in applying either Eqs. (1)–(6) or Eq. (7) to sinuous ridges is determining the channel width. For example, if the ridge width reflects the channel-belt width, rather than the channel width (Figs. 2, 3), then discharge might be overestimated.

5.2. Process sedimentology

To test methods that estimate river discharge relying on ridge geometry alone, we built on well-established previous work in physical sedimentology (Mohrig et al., 2000; Wilkerson and Parker, 2011; Trampush et al., 2014) to develop a paleo-hydraulic method that is independent of ridge morphology. The most straightforward paleo-channel parameters that can be inferred from outcrop observations are median grainsize and channel depth, reconstructed from thicknesses of sets of cross-strata. Fluvial bars grow to a height approximately equivalent to the channel depth, and therefore the thickness of fully preserved bar clinoforms, where available, should closely approximate the channel depth (Mohrig et al., 2000; Hajek and Heller, 2012). We found bar set thicknesses were 1–2.5 m (Fig. 8; Table S2), indicating the rivers were relatively shallow. Dune-scale cross sets are more abundant, and the mean dune-set thickness within channel deposits (t_d) can be related to the original dune heights (h_d) by (Paola and Borgman, 1991; Leclair and Bridge, 2001)

$$h_d/t_d = 2.9 \text{ (bounds:2.2–3.6)} \quad (8)$$

where 2.9 is the mean and the bounds represent their reported expected range. To relate channel depths (d) to dune height (h_d), Bradley and Venditti (2017) found that rivers with depths < 2.5 m had a ratio of $d/h_d = 3.5$. Because our observations of bar set thicknesses were < 2.5 m and because bars are thought to be a more reliable indicator of flow depth than dunes (Mohrig et al., 2000; Hajek and Heller, 2012), we used their shallow river relation

$$d/h_d = 3.5 \text{ (bounds:2.1–9.9)} \quad (9)$$

where 3.5 is the mean value and the bounds represent the 5%–95% range of their data. If we were to use instead the general relation of Bradley and Venditti (2017) for all rivers, this would shift our estimated mean flow depths for the Green River site up by a factor of ~2, which is relatively small compared to the uncertainty in other parameters and within the bounds evaluated for Eq. (9). We made multiple measurements of dune cross-set thicknesses in the caprock of each ridge (Table S2; Section 4), and used the mean values to calculate paleo-channel depths from Eqs. (8) and (9). We estimated the 5% and 95% uncertainty bounds on the paleo-channel depth using reported bounds on Eqs. (8) and (9) and standard Gaussian error propagation.

To reconstruct channel width independent of the ridge width, we assumed a single-thread channel based on our field observations at the Green River site (Section 6), and used the median ratio of width to depth from the Trampush et al. (2014) global compilation of bankfull channel geometry:

$$w/d = 18 \quad (10)$$

Braided rivers can have much wider channels, which, for those cases, would make Eq. (10) a conservative lower bound. To reconstruct bed slope, S, we used a dimensionless empirical relation between bankfull Shields stress and particle Reynolds number $Re_p = (Rg\,D_{50})^{1/2}\,D_{50}/\nu$ after the methodology of Paola and Mohrig (1996), Wilkerson and Parker (2011) and Lynds et al. (2014),

$$\tau^* = 17\,Re_p^{-1/2} \quad (11)$$

based again on the global compilation of single thread rivers from Trampush et al. (2014), where $\nu = 10^{-6}$ m^2/s is the kinematic viscosity of water. Eq. (11) can be combined with Eq. (3) and rearranged to solve for channel slope with known values of R, g, D_{50} and d. For D_{50}, we used the average of many median grain size measurements from each ridge caprock. Finally, we used these estimates of channel depth, slope, and width and Eqs. (1)–(6) to calculate paleo-river discharge. The uncertainty in channel width, slope, and discharge from the sedimentology-based reconstructions was assessed by propagating the uncertainty in paleo-channel depth (from Eqs. (8)–(9)) through the calculations (Eqs. (1)–(6), (10)–(11)) using Gaussian uncertainty propagation.

The equations in the sedimentology approach (Eqs. (8)–(11)) were derived using physics-based, dimensionless parameters that explicitly incorporate g and R, and are known to control sediment transport

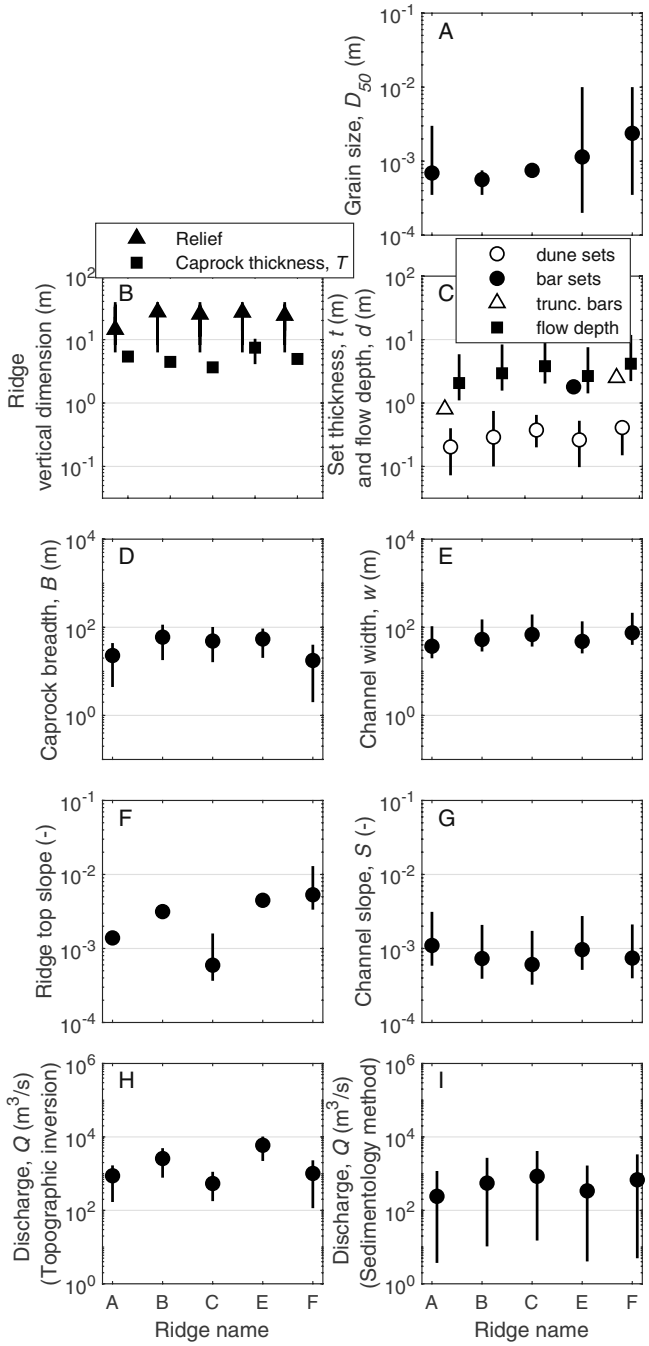

Fig. 8. Ridge parameters and paleo-hydraulic reconstructions. Symbols represent mean values (geometric mean for grain size) and lines span 5th–95th percentile of the distribution. Left column: Distribution of parameters for ridge morphology (panels B, D, F) and the associated water discharge reconstruction (H) assuming topographic inversion (see Section 5.1). Uncertainty on relief (panel B) and breadth (D) are the 5th–95th percentile of the data distribution; uncertainty on slope (F) is the 5–95% confidence interval of a least-squares linear regression; uncertainty on discharge reconstruction (H) using Gaussian uncertainty propagation from caprock breadth. Right column: measured caprock median grain sizes (A), measured dune- and bar-set thicknesses, and reconstructed flow depths from dune cross sets (C), and reconstructed bankfull paleo-channel width (E), channel-bed slope (G) and water discharge (I) using the sedimentology reconstruction method (Section 5.2). Uncertainty on grain size (panel A) is the 5th–95th percentile range of the measured median grain sizes. Uncertainty on depth (C) is combined from uncertainty in the expected range of the ratio of dune height to dune set thickness (Eq. (8); Leclair and Bridge, 2001), and 90% range of the ratio of dune height to channel depth for small channels (Eq. (9); Bradley and Venditti, 2017). Uncertainty in width (E), slope (G), and discharge (I) are estimated from Gaussian uncertainty propagation of the 5% and 95% bounds on reconstructed paleo-channel depth.

physics in rivers (Garcia, 2006; Parker et al., 2007; Wilkerson and Parker, 2011). For example, Eq. (11) is the dimensionless version of the relations for bankfull Shields stress given by Trampush et al. (2014) that explicitly includes gravity, fluid, and sediment properties. Moreover, the empirical fits are based on a large data compilation of terrestrial river channels (Trampush et al., 2014), which spans a wide range of climates and environments and is commonly used to benchmark theory in fluvial geomorphology. While these equations have been little tested outside of Earth-like conditions, the approach to characterize fluvial systems through non-dimensionalization has been shown to be robust in physical experiments and models across a wide range of fluid and sediment properties (e.g., Southard and Boguchwal, 1990; Parker et al., 2007; Lamb et al., 2012a; Grotzinger et al., 2013). Dimensional empiricisms such as Eq. (7), on the other hand, may be problematic for application to Mars because they do not explicitly incorporate fully the dynamic scales.

6. Results

The Green River site contains several ridges, and we focused our observations on seven of the more prominent examples (Ridges A-G; Figs. 5, 6), including the 4-kilometer-long ridge E, which is the longest continuous ridge in the study area. Results herein include observations of ridge morphology, ridge caprock dimensions, ridge caprock sedimentology, ridge stratigraphy, and junctions between branching ridges to evaluate the channel- and deposit-inversion hypotheses.

Ridge geometries, sedimentological observations, and paleo-hydrologic calculations are summarized in Fig. 8, which shows the averages and 5th–95th percentile range of values for each parameter (Tables S1 & S2). The tops of the ridges are at a similar relative elevation, once corrected for tectonic tilt; most are within ~15 m of each other across the 30 km^2 study area (Fig. 5). Mean ridge relief ranges 14–27 m (Fig. 8B), though it is often asymmetric between the two ridge sides. In particular, the relief of the north slopes for the east-west-running ridges (A, C-G) is on average 21 m, whereas the south sides are on average 16 m. This asymmetry in relief is coincident with the tectonic tilt of bedding and the overall slope of the modern topography, both of which dip toward north.

Ridge caprocks are cliff-forming sandstones (Fig. 6) with mean breadths varying between 22 and 54 m between ridges, although locally breadth can reach up to 130 m (Fig. 8D) and in some locations the caprock is absent due to erosion (ridges A, C, D, E, G in Fig. 5). Caprocks range in mean thickness from 4 to 7 m (Fig. 8B). Elevation of the caprock top surface varies along a ridge by up to 5 m at a 20-meter lengthscale. Along-axis ridge-top slopes are around 0.003 m/m (Fig. 8F) with tectonic tilt removed, oriented toward north or east, although different segments within a ridge can dip opposite to each other (Fig. 5B).

Fig. 6 shows vertical stratigraphic sections and topographic profiles at representative locations along the ridges A-C, E, and F. Caprocks are composed of amalgamated beds of sandstone, pebble conglomerate with clasts up to 3 cm, and occasional mudstone lenses (Fig. 9) that together have a median grainsize of medium to coarse sand (Fig. 8A). Sandstone beds are composed of medium to coarse sand and contain abundant sets of dune trough cross-stratification that range in thickness between 0.07 and 0.8 m, with averages for each ridge between 0.2 and 0.4 m (Fig. 8C). Along ridge tops, dune trough stratification is visible in planview as rib-and-furrow structures (Fig. 7C), indicating paleo-flow directions generally along ridge axes, which is consistent with the cross-sectional-view cross-strata dip directions (rose diagrams in Fig. 5A). We identified fifteen examples of truncated bar-scale inclined stratification (e.g., Figs. 7F, 9A, B, 8C), which ranged from 0.5 to 2.5 m, and two examples of fully preserved bar sets 1.8 m thick (Figs. 6, 8C). Most caprocks are composed of multiple sets of bar-scale inclined strata (multiple stories) that have migration directions oblique to dune migration directions (Figs. 5A, 6, 9A, B).

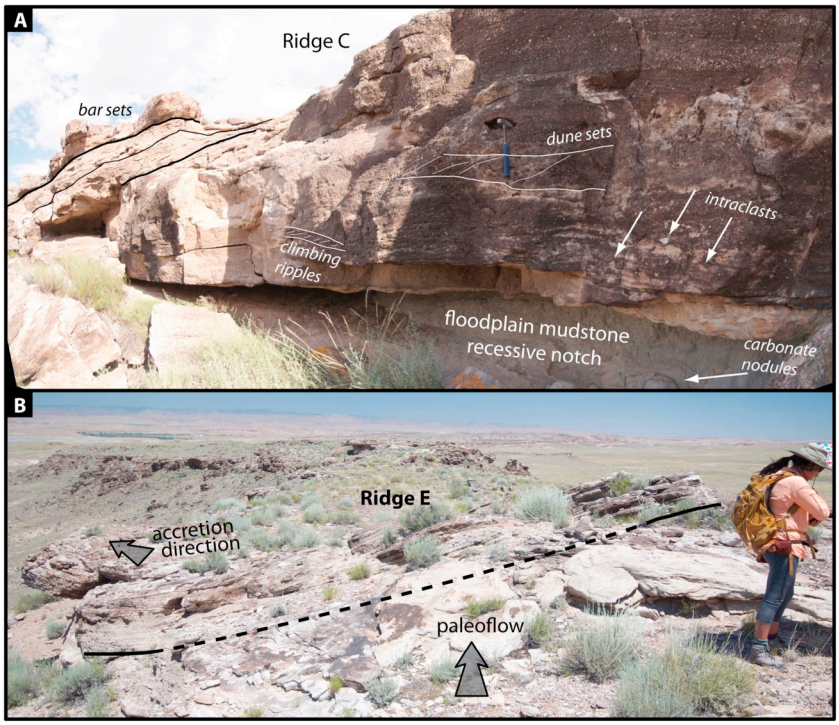

Fig. 9. Ridge caprocks and their sedimentary structures. A) Caprock of ridge C exhibiting bar-scale inclined strata, dune cross sets, climbing ripples, and mud intraclasts in the sandstone/conglomerate caprock, which overhangs an erosional niche of mudstone exhibiting carbonate nodules. Note that the bar strata indicate an accretion direction oblique to the caprock axis and almost perpendicular to the paleo-flow direction indicated by dune sets. Hammer in foreground for scale, approximately 0.3 m. Photo location indicated in Fig. 10C. B) Caprock of ridge E, showing bar strata indicating accretion nearly perpendicular to the flow direction inferred from dune migration. We interpret the strata as representing a bank-attached laterally accreting channel margin. The associated channel fill is not preserved and must have been adjacent to the modern ridge caprock (e.g., Fig. 2B). Photo location indicated in Fig. 11A.

The caprock sandstones and conglomerates unconformably overlie mudstones, and often have centimeter- to decimeter-scale mud rip-up clasts and coarse (2 cm) pebble lags present in the lower caprock strata (Figs. 6, 9A). Below the caprock, ridge flanks are largely covered with talus, and limited exposures reveal abundant mudstone with occasional thin (< 0.2 m) interbedded sandstone bodies that extend for at least tens of meters laterally (Figs. 6, 10A). The mudstones are purple to white, friable, and contain abundant decimeter-scale nodules (Fig. 9A). Thin sandstones are composed of fine to medium sand, and are planar laminated or contain centimeter-scale current-ripple cross stratification that indicate paleo-flow directions away from the ridge axes (Fig. 6). Root casts, mud cracks, and burrows are present in some of the thin sandstone sheets. At one location with better exposure (Ridge E, stratigraphic section 4; Fig. 6), three thicker (1–2 m) sandstone bodies are present in the lower parts of the ridge, with dune- and bar-scale inclined strata of medium-to-coarse sandstone, which is similar to that in the caprock. Paleo-current indicators for these lower sandstone bodies are toward 090 (Fig. 6), which is similar to the caprock paleo-current indicators from dune cross strata and consistent with the caprock axis orientation.

We analyzed three ridge junctions with detailed field observations and the high-resolution stratigraphic model to determine if they represent a bifurcation or avulsion in a coeval channel network, or a crossing of sandstone bodies that are stratigraphically distinct (Fig. 10). At the junction between ridges B and C, the caprock of ridge C intersects below the caprock of ridge B at a distinct stratigraphic level, as noted in Williams et al. (2009). The two caprocks have nearly perpendicular paleo-flow indicators and are separated vertically by 2 m of mudstone at the junction, indicating that the sandstone bodies are not coeval (Fig. 10B). Similar relationships are apparent at the junction between ridge C and an unnamed ridge to its north, with the unnamed ridge occurring approximately 10 m lower in stratigraphic section (Fig. 10C). Other ridge junctions are not as clear; ridge F splits with both branches at similar stratigraphic levels (within the 5 m of vertical variability seen in individual caprocks), and appear to represent a "Y" junction, with branches opening in the downstream direction (Fig. 10A). Cover and erosion across the center of the junction obscures the ridge relationships but the similarity between the two ridges in stratigraphic level, grain sizes and sedimentary structures, and the acute angle between paleo-current indicators, suggests that the Y-junction could represent branching of coeval river deposits.

Fig. 8 shows results from the paleo-hydraulic reconstruction techniques based on the sedimentology (inputs of dune-set thickness and grain size, using Eqs. (1)–(6), (8)–(11)) as compared to the ridge parameters and reconstructions assuming channel inversion (inputs of mean ridge thickness, mean ridge breadth, and ridge best-fit slope, using Eqs. (1)–(6)). Based on the dune cross strata, the computed paleo-channel depths were within 2.1–4.2 m, which were generally consistent with, but in cases larger than, the thicknesses of fully preserved bar clinoforms (1.8–2.5 m) where they occurred (Fig. 8C). Using the sedimentology method and the dune-derived depths, paleo-channel widths were 37–75 m (Fig. 8E) and bed slopes ranged from 0.0006 to 0.001 (Fig. 8G). These paleo-channel dimensions are smaller than the caprock dimensions, which had maximum thicknesses of 4–10 m (Fig. 8B) and maximum breadths of 45–130 m (Fig. 8D). The caprock top slopes are up to a factor of 4 times greater than the estimated paleo-channel-bed slope (Fig. 8F), and in cases indicate flow opposite in direction to the paleo-currents inferred from dune migration direction (e.g., Ridge G, Fig. 5). Discharge estimated using mean values in the channel inversion interpretation (Q = 500–6000 m^3/s) (Fig. 8H) overestimates discharge reconstructed by sedimentology (Q = 240–850 m^3/s) (Fig. 8I) by a factor of 1–20. These discharge reconstruction techniques, their uncertainties, and application to Mars are discussed in more detail in the next section.

7. Discussion

7.1. Depositional environment of ridge-forming strata

The ridge caprocks at the Green River site are composed of fluvial channel-belt deposits. Based on the thicknesses of bar and abundant dune stratification, the paleo-river channels had depths of a few meters with beds composed of sand and occasional gravel. Due to common three-dimensional exposures, we were able to identify bar-scale clinoforms with accretion directions oblique-to-perpendicular to the paleo-flow directions (Figs. 5A, 9A, B), interpreted from the orientation of

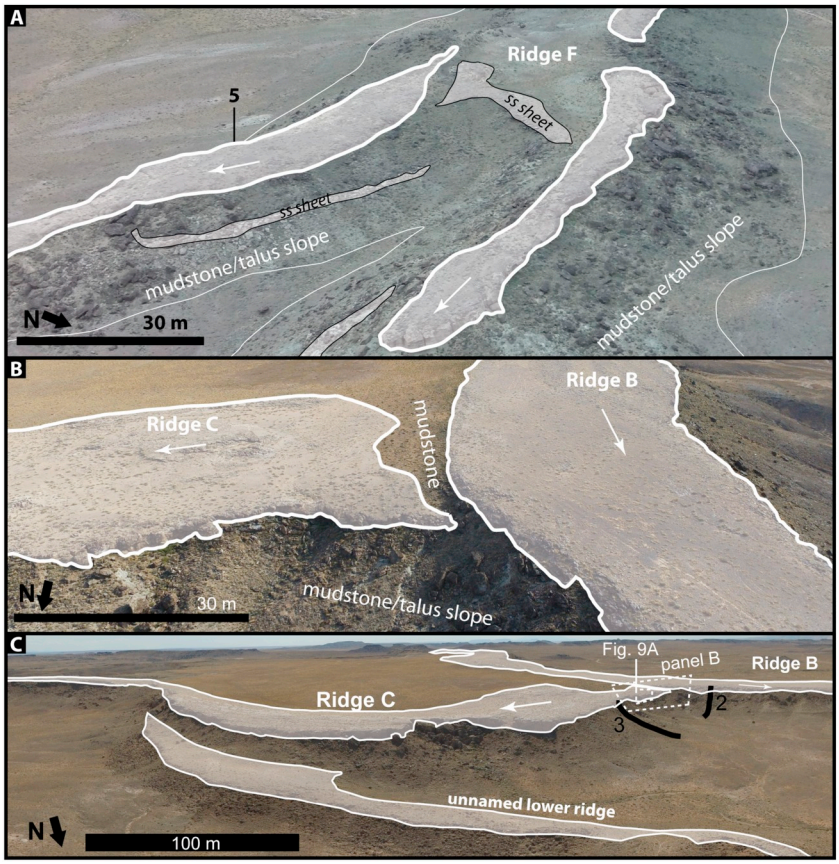

Fig. 10. UAV panoramas of three ridge junctions. In all panels sandstone bodies are shaded in white, caprock-forming sandstone bodies are outlined in a thick white line, non-caprock-forming sandstone bodies are outlined in a thinner black line, paleo-flow directions of the caprocks are given by arrows. A) Oblique quadcopter view looking southwest at the Y-junction in ridge F. The caprocks of the two branches are at indistinguishable stratigraphic positions and the caprock is eroded away at the ridge junction so it is unclear if the junction represents bifurcating sandstone bodies or a once-continuous sandstone body that has been dissected into a Y shape. Thin sandstone sheets outcrop below the caprock and do not form ridges. Stratigraphic section 5 labeled. B) Oblique quadcopter view looking south at the Y-junction between ridges B and C. The base of the caprock of ridge B is separated from the top of the caprock of ridge C by two meters of mudstone and the ridges contain paleo-flow indictors nearly perpendicular to each other. C) Oblique, southwest-looking quadcopter panorama view of ridge C and its intersections with an unnamed lower ridge and ridge B. The unnamed lower ridge is separated from the caprock of ridge C by about 10 m of mudstone. Stratigraphic sections 2 and 3, and locations of Figs. 9A and 10B are indicated.

dune trough-cross-strata and rib-and-furrow structures (Fig. 7), suggesting that the bars were laterally accreting and downstream migrating (e.g., Miall, 1994; Ielpi and Ghinassi, 2015; Wang and Bhattacharya, 2018; Nuse, 2015). We did not find evidence for laterally extensive, fining-upward accretion sets typically associated with point bars or channel cutoffs typical of fully meandering rivers (Miall, 1996). We also did not observe evidence for mid-channel bars typical of braided rivers (Best et al., 2003; Bridge and Lunt, 2006). Instead, we interpret the bar strata as downstream-migrating bank-attached free bars and channel-margin lateral accretion deposits within a low-sinuosity, single-thread, laterally migrating channel, rather than point bars within a meandering river (e.g., Okolo, 1983; Olsen, 1988; Bridge et al., 1986). The spread of dune migration directions was also low (Fig. 5A) and consistent with flow patterns within low-sinuosity channels rather than high-sinuosity meanders (Bridge, 2003).

Most of the strata underlying ridge caprocks is interpreted as floodplain deposits, similar to previous work (Williams et al., 2009; Nuse, 2015), and root casts, carbonate nodules, burrows and well developed soils suggest that the land surface was frequently subaerially exposed. Garrison et al. (2007) found two laterally extensive calcareous paleosol beds elsewhere in the Ruby Ranch Member that each are interpreted to represent tens of thousands of years of soil development. Interspersed thin, rippled sandstone sheets (e.g., Fig. 10A) likely represent channel-proximal overbank deposits, such as crevasse splays (e.g., Mohrig et al., 2000).

The ridge-capping sandstone bodies are 1.5 times thicker (range: 1–5) than the inferred channel depths (Fig. 8) and are composed of amalgamated bar and dune strata indicating that the fluvial deposits are eroded remnants of channel belts that record the migration and aggradation of a river channel across its floodplain. Paleo-flow indicators within the caprock sandstones approximately match the orientation of the ridge axes, suggesting that the ridges align roughly with the channel-belt orientations (Fig. 5A). Sandstone body thickness, T, a few times greater than paleo-channel depths, d, is typical of channel-belt deposits in general (Mohrig et al., 2000; Jobe et al., 2016) and arises because of the general tendency for rivers to avulse and abandon the channel belt after a critical amount of aggradation, which scales with the channel depth (Bryant et al., 1995; Mohrig et al., 2000; Slingerland and Smith, 2004; Jerolmack and Swenson, 2007; Hajek and Wolinsky, 2012; Ganti et al., 2014a, 2014b). Our finding of $T > d$ is strong evidence that the caprocks are remnants of channel belts, with aggrading and laterally migrating channels, consistent with the deposit-inversion hypothesis. Evidence for deposits that record lateral channel migration, typical of channel belts, comes from bar-scale inclined strata that dip oblique to the paleo-flow direction, inferred from dune strata, indicating channel-margin migration (Fig. 5). Channel-margin lateral accretion sets can extend across the entire breadth of a ridge (Fig. 9A, B), indicating that the channel deposits were more extensive prior to exhumation, and that the channel at the leading edge of the channel-margin bar would have been located laterally beyond the current extent of the ridge caprock (Fig. 2B). The exposed bar and dune strata along the caprock sides (Figs. 7, 9), and the absence of a lateral contact between channel-margin deposits and floodplain facies, further emphasizes that the caprock is an eroded channel-belt deposit and not a channel fill. We did not identify channel-fill deposits, such as finer grained lenticular bodies that would indicate decreasing flow energy in a progressively abandoned channel (e.g., Bridge, 2003; Blum et al., 2013); instead, bedform sizes and grain sizes were similar throughout the thickness of the caprocks (Fig. 6), consistent with aggradation within a channel belt.

The ridges also are not casts of river channels, but instead contain a thick sequence of fluvial channel-belt and overbank deposits (Fig. 6). Ridge relief far exceeds the inferred channel depth (Fig. 8B, C), and instead is likely set during exhumation by the relative erodibility of the caprock relative to neighboring floodplain mudstones. The strata in the ridges represent net deposition over significant time, rather than

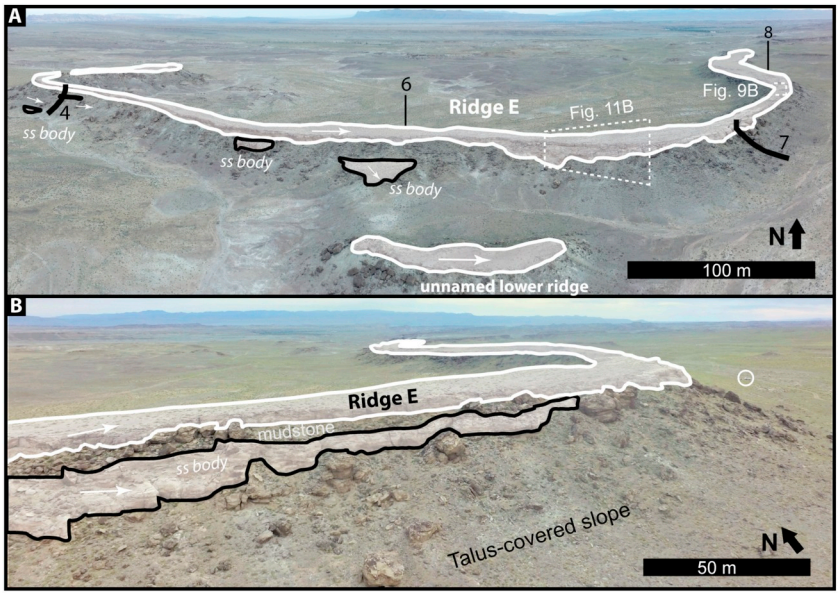

Fig. 11. UAV panoramas of ridge caprocks that have underlying non-ridge-forming channel bodies. In all panels sandstone bodies are shaded in white, caprock-forming sandstone bodies are outlined in a white line, non-caprock-forming sandstone bodies are outlined in a black line, paleo-flow directions of the caprocks are given by arrows. A) Oblique quadcopter panorama looking north at ridge E. Ridge E contains several lower sandstone bodies that do not form ridges. Sandstone bodies associated with stratigraphic section 4 have paleo-flow indicators with similar directions to those in the caprock, while sandstone bodies associated with stratigraphic section 6 have inferred paleo-flow directions nearly perpendicular to those in the caprock (Fig. 6). Another stratigraphically lower ridge occurs adjacent to ridge E and has inferred paleo-flow directions equivalent to those in ridge E. Locations of stratigraphic sections 4, 6–8 and Figs. 9B and 11B indicated. B) Oblique quadcopter photo looking northeast at ridge E. A lower sandstone body, separated from the caprock by mudstone, parallels the caprock for part of its extent and contains paleo-flow indicators aligned near those of the caprock.

preservation of a geomorphic surface. One can estimate the minimum time represented as tens of thousands of years based on the presence of paleosols (Garrison et al., 2007), and a maximum duration of several millions of years based on ages of volcanic ash within the Ruby Ranch stratigraphy (Ludvigson et al., 2015; Garrison et al., 2007; Fig. 4). Some of the ridge caprocks intersect at distinct stratigraphic levels with perpendicular paleo-flow directions (Fig. 10B, C), and thus indicate exhumation of a depositional basin with multiple generations of stacked channel belts and floodplain deposits, rather than an inverted geomorphic surface. Ridge E shows two examples where sandstone bodies underlying the caprock are laterally continuous along the ridge (Fig. 11A, B; stratigraphic section 4 in Fig. 6) and have paleo-current directions similar to the caprock, suggesting similar channel-belt orientations at different time periods. Similar observations of channel-belt stacking on Mars have been taken as evidence that ridges are deposits within a broader incised valley that has guided channel-belt orientations (Cardenas et al., 2017). However, other ridge strata in Utah contain sandstone bodies below the caprock with paleo-currents oriented oblique-to-perpendicular to the caprock paleo-currents (Fig. 11A; stratigraphic section 6, Fig. 6), which does not fit with an incised valley model for this location. Moreover, not all sandstone bodies form ridges, and in most cases the underlying sandstone bodies are only preserved beneath ridge-forming caprocks (Figs. 10A, 11A, B), suggesting that the exhumation process has led to preferential preservation of underlying sandstone bodies that align with ridge-forming caprocks.

The visual alignment of ridges C, D, E, G led previous workers to hypothesize that they were once connected, forming a sandstone body at least 10 km in length (Harris, 1980; Williams et al., 2009). We found that paleo-flow directions are consistently to the east along these ridges, and caprock thicknesses, widths, stratigraphic position, and sedimentology are as consistent between these ridge caprocks as they are within a single ridge (Figs. 5, 6). Therefore, we concur that the caprocks of E-W trending ridges C, D, E and G are part of a single sandstone channel belt that has been dissected by erosion (Fig. 12A). We additionally find that this channel belt is at the same stratigraphic level as the caprocks of Ridge F and other ridges to the southwest. N-S trending ridges A and B sit at a higher stratigraphic level than ridge C-D-E-G, which is confirmed by intervening floodplain facies between the caprocks of ridges B and C (Fig. 10B). There are several smaller, stratigraphically lower ridges with paleo-currents that differ significantly from the upper ridge caprocks, suggesting that channel-belt orientations were different in the lower part of the ridge-forming stratigraphy (Figs. 5A, 10, 11, 12A).

Although most ridge junctions represent caprocks intersecting at different stratigraphic levels, in some cases caprocks do appear to bifurcate (Fig. 10A). These examples may represent deposits from a coeval network of channel belts, which either bifurcate or are abandoned through avulsions. However, due to the eroded state of the ridges, it is also possible that some of the caprock bifurcations at the same stratigraphic level result from erosion of a notch during exhumation that has split a single sandstone body that was once more laterally extensive, or from two crossing caprocks that are amalgamated at the junction with poor preservation of the junction stratigraphy. For these cases, remote sensing was not enough to distinguish different stratigraphic levels, and even detailed field analyses could not verify the origin of the ridge bifurcation.

7.2. Ridge exhumation and degradation

The variability in caprock thicknesses and breadths along a given ridge is due in part to erosion. Abundant talus blocks of caprock material, up to 5 m in diameter (Fig. 13), indicate that caprock sides are actively backwasting, and differences in extent of backwasting can lead to large variations in caprock breadth over short distances (Fig. 13A) even to the point where a mudstone ridge is only partially covered by caprock (Fig. 13B). Often there is a recessive notch, decimeters in height, that undercuts the mudstone directly below the caprock, creating overhangs ~1 m in scale (Figs. 9A, 13C). Talus production through caprock undermining likely armors the underlying mudstone and may set the pace of lateral escarpment retreat (Ward et al., 2011).

Caprock thicknesses are also variable along a ridge (Figs. 6, 8B), and field observations show that the ridge surface cuts across different stratigraphic levels indicating some top-down erosion (Figs. 5B, 13B), similar to observations on Mars (DiBiase et al., 2013). We infer that variability in ridge-top profiles is due to erosion, in addition to uncertainty in correcting for tectonic tilt and local deformation, resulting in ridge-top slopes that locally change dip directions and can be opposite of the paleo-flow direction inferred from bedforms (Fig. 5B).

Deposit inversion in Green River appears to occur because of the resistance of thick sandstone bodies to erosion, as compared to thinner sandstone bodies and mudstone. Bimodality in grain size of this type is typical of lowland fluvial systems where floodplain facies are dominated by fine-grained overbank deposits and channel-belt deposits are sandy (e.g., Heller and Paola, 1996). In the case of the Green River site, the mudstone is friable, whereas sandstones are better cemented and

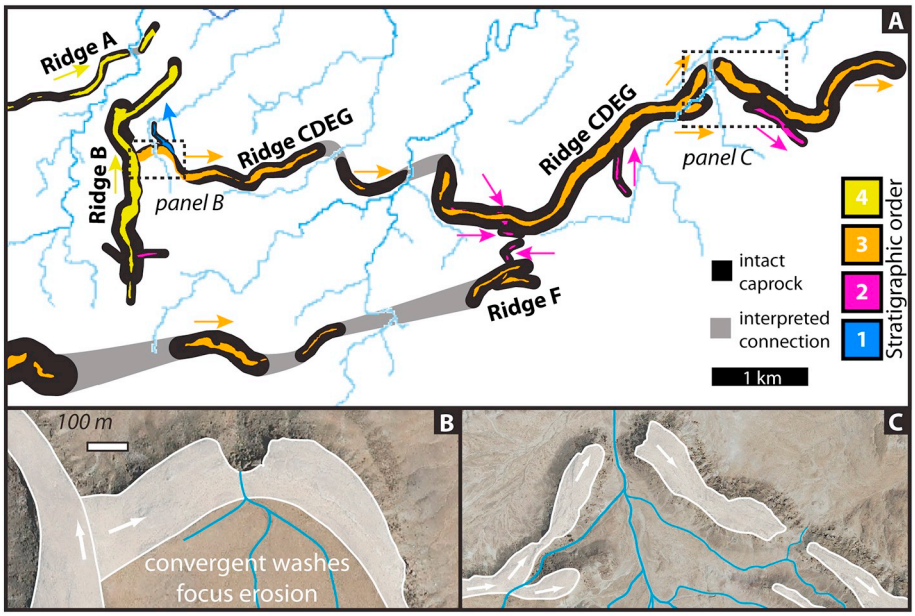

Fig. 12. Interpreted ridge segment connections and erosion by modern washes. Locations of panels B and C are shown in panel A. A) Interpretation of ridge connections, relative stratigraphic positions, paleo-flow directions, and networks of modern washes (blue lines). Ridges C, D, E and G are inferred to be remnants of a larger channel-belt sandstone body. Ridge B, which appears to be at a similar stratigraphic level as Ridge A, superposes Ridge C (Fig. 10B). Modern washes preferentially bisect the ridges where they are convex in the direction of down tectonic dip. B) Modern wash partially eroding through a caprock by accumulating flows from a plateau on the up-dip side and focusing them across a single area that currently stands as a waterfall. C) Fully developed ridge bisection. (For interpretation of the references to color in this figure legend, the reader is referred to the web version of this article.)

form vertical cliffs. However, not all sandstone bodies form ridges (e.g., Fig. 11). Our qualitative observations suggest no significant difference in grain size or hardness between ridge-forming and non-ridge-forming sandstone bodies. Instead, ridge-forming caprocks tend to be the thickest sandstone bodies in the field area, often exceeding 3 m, whereas non-ridge-forming sandstone bodies are typically thinner. Thicker caprocks may be needed to generate sufficient talus to armor the slope and slow its erosion (Ward et al., 2011).

The gaps between the E-W trending ridges C, D, E, G, which we infer to once have been a connected sandstone body, align with modern washes (Fig. 12A). These washes drain to the north, perpendicular to the trend of the ridges, until they encounter a ridge, at which point they turn to run alongside the ridge until a gap allows flow to the north again. Because tectonic tilt of the bedding is to the north, the southern parts of the caprock would have been exhumed first, thus guiding the washes to the gap locations and producing focused fluvial incision during subsequent ridge excavation. This hypothesis explains why the gaps between ridges occur on what would have been curved ridge segments that are convex to the north; these segments would have been the last to be exhumed and water would have been funneled across them. Ridge C shows an example of a north-convex point being incised by a modern wash (Fig. 12B), and the gap between ridges E and G exemplifies that process when complete (Fig. 12C).

7.3. Evaluating paleo-hydraulic reconstructions for exhumed channel belts

The ridges at the Green River site contain a thick sequence of fluvial floodplain and channel-belt deposits that record a rich history of fluvial activity over millions of years. Channel fills are rare, and instead the sandstone bodies record the extent of channel lateral migration and aggradation, consistent with deposit inversion. The ridge-forming caprocks tend to represent thicker, amalgamated channel-belt sandstones, and erosion during exhumation has removed much of the neighboring floodplain material and thinner channel-belt sandstones, except where they are shielded below more resistant caprocks, making the ridge network an incomplete representation of the original stratigraphic architecture of the depositional basin. Moreover, the ridge-forming channel-belt sandstones are heavily degraded, largely by lateral

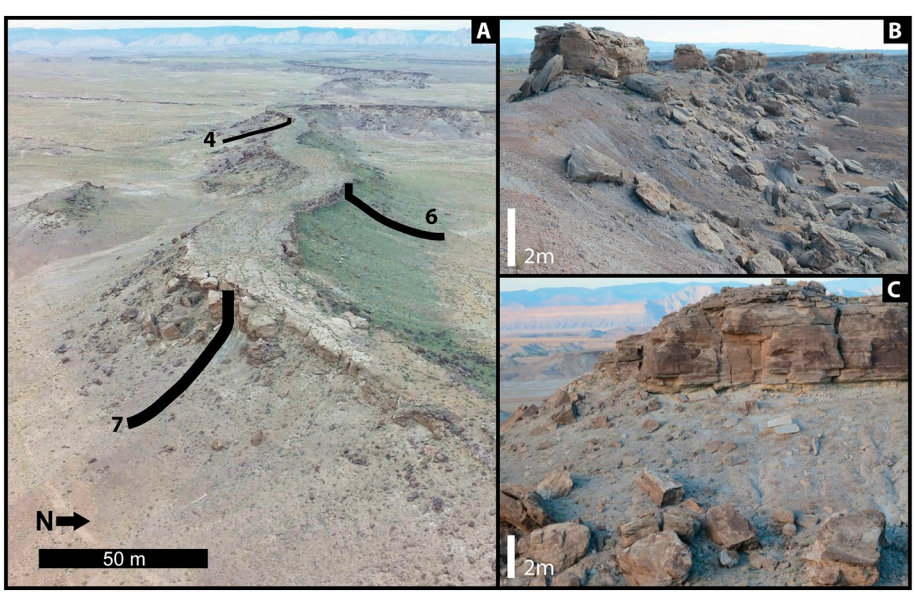

Fig. 13. Examples of ridge erosion by scarp retreat. A) Oblique quadcopter view looking west at ridge E, with stratigraphic sections 4, 6, and 7 indicated. The ridge flanks are armored with talus generated from the caprock, with little talus evident between ridges. Differing extents of scarp retreat can lead to large changes in caprock breadth over short lateral distances, as is evident near the top of section 7. B) Caprock backwasting and talus generation significantly affects caprock breadth, but can leave thickness largely preserved. Note the thick caprock blocks left in places along a ridge where all the neighboring caprock has totally been eroded. Photo looking east on ridge A. C) Thick caprock generates large talus blocks comparable to the full thickness of the caprock, again indicating that caprock thickness degrades significantly slower than the breadth. Photo looking northeast at the northernmost ridge in panel 12C (ridge G, at the location where it is bisected by a wash).

backwasting, making the original channel-belt extents unknown. Because channel fills are typically fine grained (e.g., Bridge, 2003; Reijenstein et al., 2011; Musial et al., 2012) it is likely that any channel fills that existed were eroded along with the fine-grained floodplain material. Sandstone bodies have been dissected by erosion, and ridge junctions often form because of caprocks intersecting at distinct stratigraphic levels, and thus they do not represent an exhumed river network. Together, these observations at Green River are consistent with the deposit inversion model proposed by DiBiase et al. (2013) and demonstrate the uncertainty in applying paleo-hydraulic techniques that assume channel inversion.

Using the sedimentology reconstruction as a baseline, we find that caprock average thickness, breadth, and along-axis slope tend to exceed the inferred paleo-channel depth, width, and bed slope, and so using those ridge parameters directly in Eq. (1)–(6) under the channel-inversion hypothesis overestimates the paleo-discharge by a factor of 1–20 (Fig. 8H, I). If ridge breadth and thickness values larger than the average were used instead in an attempt to account for ridge erosion (e.g., Williams et al., 2009 used third quartile), the paleo-discharge could be overestimated by a factor up to 50. Likewise, caprock breadths are vanishingly small in other places due to erosion (Figs. 8D, 13), making inferring channel width from ridge width ambiguous. Using ridge slope as an estimate for channel slope was found to have the largest contribution to the overestimation of discharge, and in cases the ridge top slopes, even after being corrected for tectonic tilting, indicate opposite paleo-current directions (Fig. 5B). Opposition of ridge-top and paleo-channel slopes has also been observed on Mars (DiBiase et al., 2013; Lefort et al., 2015).

In comparison to previous work at the Green River site, Williams et al. (2009) used empirical relations for river discharge that rely on measurements of river width alone, similar to Eq. (7), assuming that channel width is represented by the third quartile of the maximum measured ridge breadth, and found $Q = 370$ and 350 m^3/s for our Ridges B and E (their D and B, using Osterkamp and Hedman (1982)). Although their estimate of discharge based on ridge width is similar to ours based on sedimentology ($Q = 550$ and 340 m^3/s median values for our Ridges B and E), we caution that the correlation between ridge width and paleo-channel width is unlikely to be generally applicable to ridges on Mars. If the ridges are exhumed channel belts as they are in Green River, not inverted channel fills, then the caprock breadth reflects the extent of river lateral migration within a larger channel belt, modified by erosion, rather than the channel width. We are not aware of a reason why eroded channel belt widths should correlate with channel widths. The end member scenario of very narrow channel belts, referred to as ribbon sandstone bodies (e.g., Friend et al., 1979), might produce sand bodies with breadths that are similar in scale to the channel width. Ribbon sandstones could potentially explain the consistency between ridge-based and sedimentology-based discharge reconstructions at the Green River site, but this idea is difficult to evaluate given the eroded state of the ridges. Nonetheless, more generally, it is well documented that channel-belt widths, for a given channel size, can vary by several orders of magnitude (e.g., Robinson and McCabe, 1997; Jerolmack and Mohrig, 2007; Jobe et al., 2016; Fernandes et al., 2016).

To expand our analysis to channel belts outside of the Green River site, Fig. 14A shows a large compilation of data from uneroded terrestrial channel belts across a wide range of environments (Mohrig et al., 2000; Foreman et al., 2012; Zaleha, 2013; Jobe et al., 2016; Milliken et al., 2018). This compilation indicates that the ratio of channel-belt width to channel width can vary from $2 < B/w < 36$ where these bounds represent the 5th to 95th percentile of the distribution, due to varying extents of lateral channel migration. For the Green River site, the ratio of average ridge caprock breadth to estimated channel width is far smaller and varies from $0.2 < B/w < 2$ (5th–95th percentile) (Fig. 14A), consistent with narrowing of the channel-belt sandstones during ridge exhumation. To estimate the general uncertainty in inferring channel width from ridge width alone, we used the lower bound of ridge widths from Green River as a highly eroded endmember, and the upper bound from the data compilation as an uneroded endmember with extensive lateral migration. This analysis yields a potential uncertainty in the ratio of B/w spanning over two orders of magnitude ($0.2 < B/w < 36$) (Fig. 14A) due to the unknown amounts of lateral migration and erosion. As an example, work by Fernandes et al. (2016) shows that the modern channel belt on the Mississippi River is far wider than the modern channel by a factor of ~20 (Fig. 3B). Martin et al. (2018) found a similar result in a high-resolution seismic study of ancient channel belts of the Mungaroo Formation, Australia.

Williams et al. (2009) also evaluated relations based on the radius of curvature and wavelength of isolated bends at the Green River site, and extracted these values from the ridge geometry, which yielded discharges of 300 m^3/s and 500 m^3/s for our ridges B and E. Their result is consistent with ours, but again it is unclear if ridge bend wavelength serves as an indicator of channel geometry in general. If ridges are exhumed channel belts, then ridge curvature should reflect the channel-belt curvature, modified by erosion, rather than the channel pattern. Fig. 3B illustrates an example where the Mississippi river has far greater sinuosity with smaller bend wavelengths as compared to the channel belt. Similar examples also exist in seismic records of ancient channel belts (Martin et al., 2018). We are not aware of studies on the controls on channel-belt curvature. Consistency between the width-to-bend wavelength ratio for ridges as compared to meandering channels is often used to support the inverted channel hypothesis (Burr et al., 2010; Kite et al., 2015b); however, similar ratios might also exist for channel belts because both their widths and bend wavelengths are larger. Channel curvature might be inferred more directly from sets of curvilinear features in planview that appear similar to scroll bars on meandering rivers (Moore et al., 2003; Burr et al., 2009; Jacobsen and Burr, 2018), but likely represent intersection between dipping lateral accretion strata and the land surface on Mars (e.g., Jerolmack et al., 2004; Goudge et al., 2018). These features could record the channel margin geometry, but they are not apparent at the Green River site. Importantly, bend curvature correlations with discharge have been evaluated on Earth only for meandering rivers with active bend growth and cutoffs (Williams, 1988); thus, their applicability is unclear for the Green River ridges and most ridges on Mars, which have low sinuosity and lack evidence for point bars or cutoffs that would indicate meandering (see Moore et al., 2003; Kite et al., 2015b for notable exceptions). Although ribbon sandstones might have breadths similar to the paleo-channel widths, these sandstone bodies are characterized by a lack of lateral migration (Friend et al., 1979), and thus are atypical of actively meandering rivers where the discharge-bend curvature relations apply.

7.4. Paleo-hydraulic reconstruction of ridges on Mars

Detailed sedimentological observations of dune and bar strata is not possible for the vast majority of ridges on Mars, where only orbital data is available. Instead, we propose that the most reliable indicator of paleo-channel depth that can be measured from orbital data is caprock thickness. Unlike ridge width that can potentially vary by orders of magnitude for a given channel width (Fig. 14A), channel-belt thickness tends to have a relatively tight linear correlation with channel depth. Based on our large compilation of channel-belt deposits on Earth and observations for Utah ridges, the median channel-belt thicknesses and ridge caprock thicknesses, relative to channel depths, is $T/d = 1.5$, with a 5th–95th percentile range of $T/d = 0.8$–4 (Fig. 14B). Our observations of caprock thicknesses at Green River alone support a similar ratio (Fig. 14B), suggesting that top-down erosion of caprocks at Green River is small compared to backwasting that narrows ridge breadth (Fig. 14A). The correlation between channel-belt thickness and channel depth is tied to the mechanics of river avulsion, the process by which

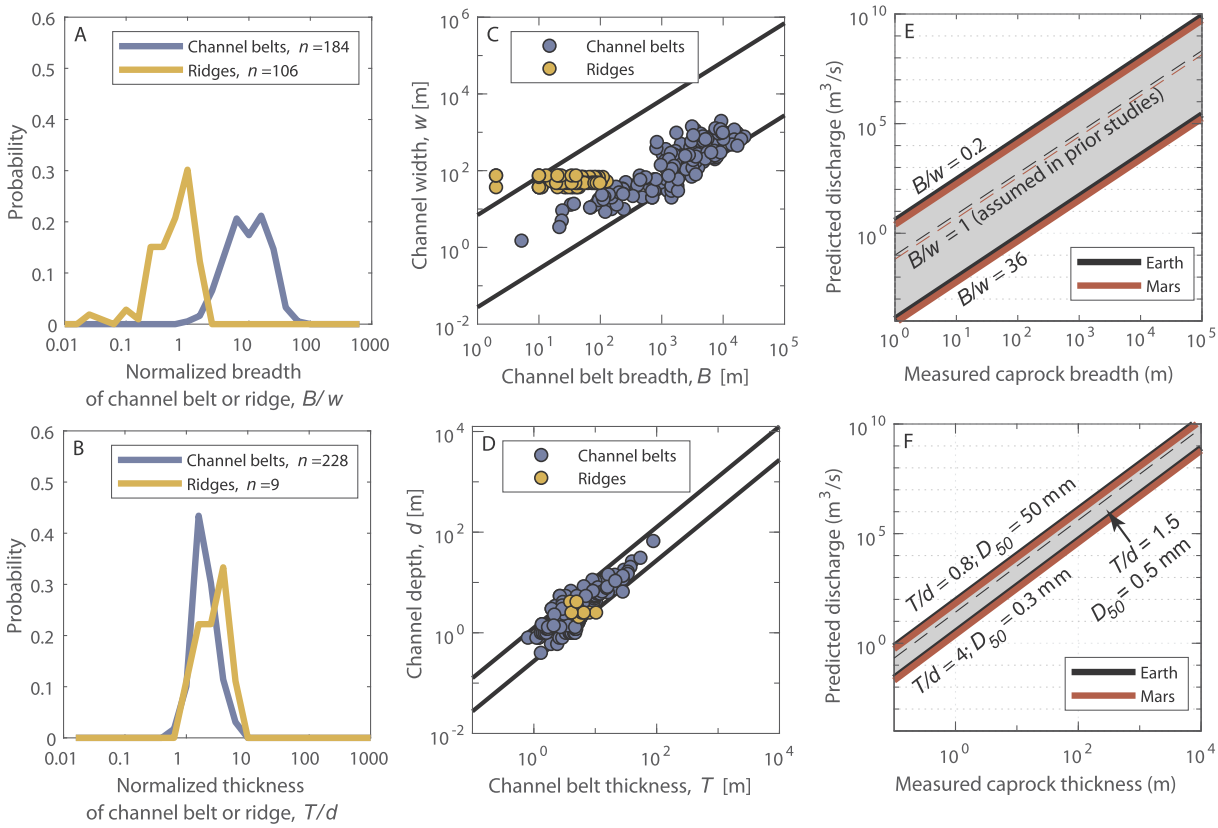

Fig. 14. Ridge, channel belt and paleo-channel parameters based on a compilation of uneroded channel belt deposits on Earth and eroded ridges at the Green River site. A) Probability density of uneroded channel-belt sandstone widths and, B) thicknesses, normalized by independently inferred paleo-channel widths and depths taken from a number of data compilations (Mohrig et al., 2000; Foreman et al., 2012; Zaleha, 2013; Jobe et al., 2016; Milliken et al., 2018). Also shown are all the measurements of ridge caprock breadth (spaced every 100 m along) and thickness (measured at each stratigraphic section) from the six studied Green River ridges, normalized by estimated average paleo-channel widths and depths using the sedimentology reconstruction method for each ridge. C and D) Data from panels A and B showing correlation between ridge or channel-belt breadth and channel width, and ridge or channel-belt thickness and channel depth. The lines represent the 5th and 95th percentile of the distribution (B/w = 0.2–36 and T/d = 0.8–4). E) Discharge reconstruction using Eq. (7) with a = 0.1 and b = 1.866 (Eaton, 2013), a relation commonly applied to ridges on Mars assuming channel inversion. The shaded gray zone, spanning a factor of over 30,000, represents the potential uncertainty associated estimating discharge from measurements of ridge width alone using Eq. (7) because of the unknown size of the channel belt, relative to the original channel, and the unknown degree of lateral erosion during exhumation (i.e., B/w = 0.2–36). Dashed line is B/w ratio of unity, which is a typical assumption in previous work. F) Our preferred method to reconstruct river discharge using caprock thickness as a proxy for channel depth (Eq. (12)). The dashed line gives the best-estimate values, using T/d = 1.5 and D_{50} = 0.5 mm as described in Section 7.4. The gray region, spanning a factor of 30, represents the uncertainty in converting caprock thickness to channel depth based on data in panels B and D, and the uncertainty in grain size by assuming representative sand and gravel end members. Red lines in panels E and F show the same discharge calculations made for martian conditions (using a prefactor = $1.257^{-1.866}$ in Eq. (7) in panel E (Burr et al., 2010); parameters g = 3.71 m/s^2, ρ_s = 3.0 g/cm^3 used in panel F). (For interpretation of the references to colour in this figure legend, the reader is referred to the web version of this article.)

rivers abruptly shift course and abandon a former channel belt. Analysis of terrestrial channel-belt sandstones, theory, and laboratory experiments indicate that avulsions tend to occur once the aggradation thickness is a small multiple of the channel depth (Bryant et al., 1995; Mohrig et al., 2000; Slingerland and Smith, 2004; Jerolmack and Swenson, 2007; Hajek and Wolinsky, 2012; Ganti et al., 2014a, 2014b). Caprock thickness, thus, represents a potentially robust metric to infer channel depth within a factor of ~2 (Fig. 14B).

Applying the method on Mars requires analysis of high resolution imagery and digital terrain models (e.g., HiRISE) to identify caprocks, measure their thicknesses, and evaluate their preservation and possible burial from talus. We suggest utilizing the common morphologic expression of sinuous ridges with cliff-forming caprocks underlain by recessive mudstones that form sloping hillsides (Fig. 15). Fig. 15B shows example topographic profiles from ridges in Utah and from a ridge on Mars (also shown in Fig. 1B) where cliff-forming caprocks are present and measureable. For the cases in Utah, the thicknesses of the cliff-forming units inferred from the topography correspond with our field measurements of caprock thicknesses (Fig. 6). In addition to using topography, Mars imagery can also reveal shadows from overhangs and a lack of talus cover to support a caprock interpretation (Fig. 15A). Given the resolution of available datasets on Mars (e.g., HiRISE stereo DEMs are reported to have <0.5 m vertical precision (Kirk et al., 2008)), caprocks at least a few meters thick should be targeted. For example, DiBiase et al. (2013) used HiRISE stereo DEMs to identify and measure the thickness of a channel-belt caprock in the Aeolis Dorsa region, Mars, and used the thickness data to calculate channel depth and river discharge, similar to our recommended approach.

Grain size is another obstacle in applying our sedimentology-based reconstruction method to Mars; however, the method is relatively insensitive to grain size (Parker et al., 2007). For example, assuming medium sand (D_{50} = 0.3 mm) versus medium gravel (D_{50} = 50 mm) introduces an uncertainty in the reconstruction of water discharge of a factor of about three. For river deltas, an additional constraint based on delta lobe size, which relates to backwater hydrodynamics, also can be used to constrain channel-bed slope or grain size (DiBiase et al., 2013).

For analysis of exhumed channel belts on Mars using available remote sensing data, we recommend the following steps: 1) Measure

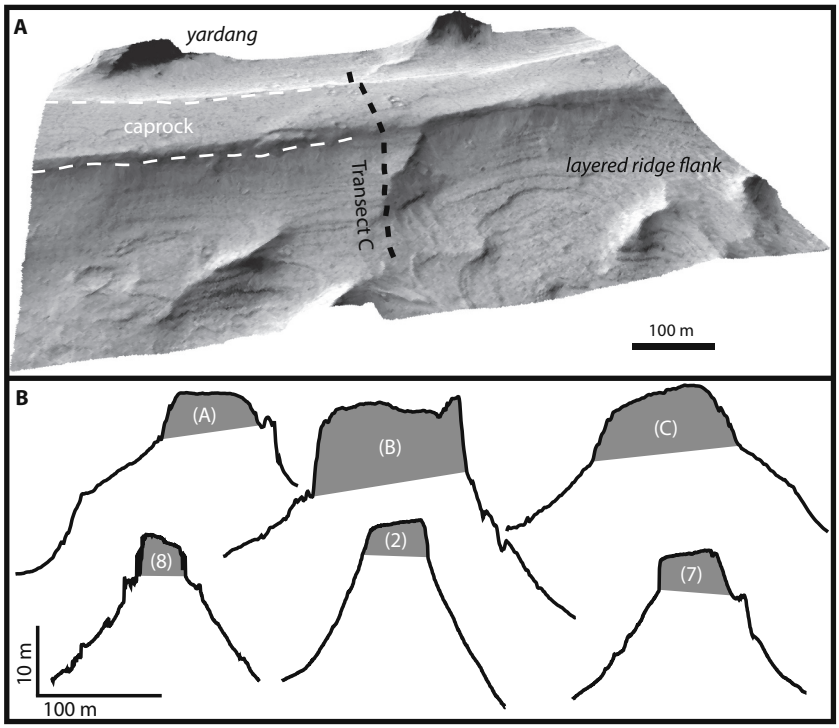

Fig. 15. A) Zoomed-in perspective view of a ridge in Aeolis Dorsa, Mars shown in Fig. 1B without vertical exaggeration (Coordinates: −6.142, 151.450). Image shows the cliff-forming caprock that casts a shadow, likely indicating an overhang, with layered rock visible below, indicating that the ridge caprock has been eroded. The caprock annotation is purposefully absent on the right side for visibility. HiRISE DEM with draped imagery using images PSP_002279_1735 and PSP_002002_1735. Courtesy Jay Dickson. B) Cross sections of ridges on Mars (top row: letters A-C with corresponding locations indicated on Fig. 1B, and transect C is also shown above on Fig. 15A) and in our Utah field site (bottom row; numbers 2, 7 and 8 correspond to stratigraphic section numbers (Fig. 6)) where profiles were taken. Photogrammetric DEMs from quadcopter photos. Scale is identical between ridges; vertical exaggeration ~5×. Ridge profiles are truncated at the base of the talus slope. The gray shaded area denotes the inferred caprock thicknesses using both the imagery (e.g., shadows) and the topography (cliff) as indicators of a break in slope at the base of the cliff-forming caprock.

caprock thickness. High-quality caprock measurements will occur where talus does not obscure the caprock and a clear cliff scarp is visible (e.g., Fig. 15). 2) Infer paleo-channel depth using the measured caprock thickness and $T/d = 1.5$, with a 5th–95th percentile range of $T/d = 0.8$–4 (Fig. 14B). 3) Make a grain size estimate. If no constraints are available, we recommend using medium-to-coarse sand ($D_{50} = 0.5$ mm), which is typical for ridges in Utah and rivers with muddy floodplains that are likely to make ridges during exhumation. Bounds for medium sand and medium gravel (0.3–50 mm) can be used for conditions typical of lowland depositional rivers on Earth (e.g., Lamb and Venditti, 2016), which introduces an additional factor of ~3 uncertainty on Q. 4) Eqs. (1)–(6), (10), and (11) then can be combined to calculate a bankfull river discharge:

$$Q = 74.2\, C_f^{-1/2}\, (Rg)^{3/8}\, \nu^{1/4} D_{50}^{1/8} d^2 \tag{12}$$

where $C_f = u^{*2}/U^2$, $u^{*2} = gdS$ for steady and uniform flow, and U can be computed from Eqs. (2)–(6) following the method of Engelund and Hansen (1967).

Fig. 14E and F show the sensitivity of the discharge reconstructions with inputs that rely on remote sensing alone for the inverted-channel method that utilizes ridge width (Eq. (7), with coefficient and exponent from Eaton (2013)) and our proposed method for deposit inversion of exhumed channel belts that utilizes caprock thickness (Eq. (12)). The largest uncertainty for the inverted channel method that utilizes ridge width alone (Eq. (7)) is the unknown ratio between ridge breadth to channel width, which can vary from $0.2 < B/w < 36$ (5th–95th percentile) for single-threaded channels due to unknown channel belt extents and ridge erosion, leading to potential uncertainty of over four orders of magnitude in discharge (Fig. 14E). Note that Fig. 14E does not account for the additional uncertainty in the assumed constants a and b in Eq. (7), which likely vary for rivers of different depth, slopes and bed sediment sizes, in addition to gravity (Section 5.1). For deposit inversion (Eq. (12)), the largest uncertainty is due to the unknown ratio between channel-belt thickness and channel depth ($T/d = 0.8$–4), and secondarily grain size (using $0.3 < D_{50} < 50$ mm), which yields an uncertainty of about a factor of 27 in discharge using Gaussian error propagation (Fig. 14F). The uncertainty associated with accurately measuring the caprock breadth or thickness on Mars is not accounted for here. The deposit inversion method has far less uncertainty due to the tight correlation between channel depth and caprock thickness, as expected due to river avulsion mechanics during channel-belt formation (Bryant et al., 1995; Mohrig et al., 2000; Slingerland and Smith, 2004). Martian gravity and basaltic-sediment density also can be explicitly incorporated in the deposit-inversion reconstruction, which shifts the discharges to slightly smaller values (Fig. 14E, F).

As an example application on Mars, we used data from DiBiase et al. (2013) because it is one of the rare studies that report caprock thickness. DiBiase et al. (2013) measured caprock thickness of ~10 m and a caprock width of ~600 m for what they infer to be a trunk channel complex (i.e., channel belt) that transitions into a series of bifurcating delta lobes in the Aeolis Dorsa region, Mars. Using their measurements and assuming a single-thread channel, we estimated a paleo-channel depth of 6.7 m (range: 3–13 m), width of 120 m (range: 49–230 m) and corresponding bankfull discharge of 2300 m^3/s (range: 370–8800 m^3/s) using $T/d = 1.5$ (range: 0.8–4), $D_{50} = 0.5$ mm, and Eqs. (10) and (12). In contrast, if the entire ridge breadth is taken to be a proxy for channel width, then the inferred channel width is 600 m and the discharge is 10,000 m^3/s using Eq. (7) with the Eaton (2013) parameters, approximately 5-fold larger than the best-estimate value using the caprock thickness approach, and similar to the peak annual flood on the Mississippi River (Lamb et al., 2012b). Complicating the interpretation of ridge breadth, the caprock from the DiBiase et al. (2013) study area also contains a number of smaller superposed ridges that have breadths ~50 m (see their Fig. 5), which yielded a discharge estimate using Eq. (7) of 97 m^3/s, a factor of 100 smaller than using the entire caprock breadth. Based on typical stratigraphic architecture of fluvial deposits (e.g., Heller and Paola, 1996; Blum et al., 2013) and the unlikely preservation of channel fills during exhumation, we suspect that the smaller ridges are still unlikely to be channel fills, but might reflect smaller amalgamated channel belts with lesser extents of river lateral migration (e.g., ribbon sandstones; Friend et al., 1979), similar to the interpretation of DiBiase et al. (2013). Regardless of the specific interpretation, this example illustrates the ambiguity of inferring channel widths and channel-belt extents from measurements of eroded caprock breadths, and how that ambiguity can result in significant uncertainty in water discharge estimates.

7.5. Implications for Mars

The inverted channel hypothesis proposes that ridges accurately reflect the geometry of river channels, preserved as a geomorphic surface in inverted relief. Instead, our observations in Utah are consistent with deposit inversion in which river lateral migration and aggradation led to the formation of channel belts that were likely wider and thicker than the original channel, but then were modified by scarp retreat during exhumation. Channel fills that preserve the original channel geometry, in contrast, are not preserved. Our global compilation of terrestrial channel belts supports the view that channel belts are often significantly wider than the original channels. Perhaps more importantly, deposit inversion indicates that substantial time is recorded in the ridge caprock and underlying strata, including multiple generations of rivers occupying a single channel belt, and multiple generations of channel belts building thick ridge-bearing strata. Reinterpreting sinuous ridges as exhumed channel belts, therefore, implies likely smaller river discharges and far greater durations of fluvial activity on Mars, potentially by millions of years.

The work of Harris (1980) at the Green River site is often used to justify the likely nature of ridges on Mars as composed of channel fills, but his terminology is different than what is commonly used today in sedimentology (which we presented in Section 2). We believe that this difference in terminology has led to misunderstanding of his results. In particular, Harris termed the ridges synonymously as channels, paleo-channels, and channel fills by definition, but then went on to define channels (or channel fills) as *a body of clastic material, regardless of size and shape, generally sandstone and/or fine conglomerate, originally deposited by rapidly flowing water in an ancient stream course, which has internal structures indicating the direction of sediment transport.* This description is equivalent to our definition of a channel-belt sandstone body, not a paleo-channel fill as we use the term. Harris divided the channel-belt deposits (his "channels fills") into what he termed point-bar and channel-fill deposits, a classification scheme that continued with Williams et al. (2007, 2009) and has been applied to ridges on Mars (Burr et al., 2010; Williams et al., 2013; Kite et al., 2015a; Jacobsen and Burr, 2017). However, Harris goes on to define point bars as lateral accretion sets, and we now recognize that downstream-migrating bars and channel migration can create lateral accretion sets in the absence of active meandering and point bars (e.g., Okolo, 1983; Olsen, 1988; Bridge et al., 1986). More importantly, Harris's description of what he calls channel fills is consistent with our definition of channel deposits that make up the channel belt. In other words, they are the trough-cross-stratified sandstone facies and lateral accretion sets that result from aggradation and lateral migration of the active river channel, rather than finer grained overbank deposits that fill and preserve the geometry of abandoned channels. Several studies cite Harris (1980) to support the idea that ridges on Mars, especially in their straight segments, are composed of channel fills that closely preserve the original channel shape (e.g., Williams et al., 2007; Williams et al., 2009; Burr et al., 2010), citing, for example, Gibling (2006) to define channel fills (e.g., Jacobsen and Burr, 2017). While Gibling's definition of channel fills is similar to ours: "the filling of a channel without change in its perimeter (banks and basal surface), for example the fill of an abandoned channel," this is inconsistent with how Harris uses the term. The differing terminology aside, Harris's description of the caprocks is similar to ours: they are composed of bar and dune strata that record the aggradation and lateral migration of the active channel to form a channel belt, rather than a channel-geometry-preserving fill.

On Mars the topographic inversion hypothesis is often implicitly assumed in order to link ridge segments together to form a river network. However, in the Cedar Mountain Formation, ridge junctions typically represent caprock sandstone bodies that intersect at distinct stratigraphic levels, and therefore were not coeval. Channel-belt thicknesses are commonly a small fraction of the total ridge relief; therefore, detecting decimeter stratigraphic offsets between adjoining ridge caprocks that we observed in Utah would be difficult by remote sensing alone. Nonetheless, larger stratigraphic offsets and caprocks crossing at distinct stratigraphic intervals are apparent on Mars (Burr et al., 2010; DiBiase et al., 2013; Kite et al., 2015a; Goudge et al., 2018) (Fig. 1B). Moreover, DiBiase et al. (2013) inferred paleo-flow directions, based on the dip of bedding, to be opposite to the orientation inferred from ridge-top slopes, and attributed this to differential erosion, similar to our observations in Utah. Although multiple episodes of channel erosion and rapid volcanic infill have also been proposed as an explanation for stratigraphically distinct ridges (e.g., Burr et al., 2009), channel-belt stacking is the primary characteristic of the architecture of fluvial sedimentary basins (Gibling, 2006; Heller and Paola, 1996), and cross-cutting ridges would be a necessary consequence of preferential erosion of floodplain deposits during exhumation. On Mars, ridges with stacked patterns are apparent for some ridges at Aeolis Dorsa (Fig. 1; DiBiase et al., 2013), Arabia Terra (Davis et al., 2016), Hypanis Valles (Fawdon et al., 2018), Gale Crater, near Juventae Chasma, Eberswalde, Hypanis Valles, and in fans on crater walls like those in Harris and Saheki Craters.

In contrast to Utah where runoff and river erosion is important in exhuming the ridges, eolian erosion appears to be the dominant exhumation process on Mars (e.g., Zimbelman and Griffin, 2010). Whereas fluvial erosion is focused in steep areas which accumulate the largest amount of water, eolian erosion may be more uniform or have a directionality associated with the dominant winds. Therefore, eolian erosion may help to explain longer ridges, more uniform ridge widths, and the preservation of more complex ridge crossing patterns observed on Mars (Burr et al., 2009; Burr et al., 2010) (e.g., Fig. 1). Uniform ridge geometries on Mars has been interpreted to indicate minimal caprock erosion (Burr et al., 2010; Williams et al., 2013; Kite et al., 2015b), but it might instead indicate a uniformity in the erosion process due to the wind. Cliff-forming caprocks are also targeted on Mars as indicators of a preserved paleo-channel width (e.g., Burr et al., 2010) because Harris noted that exhumed channel fills (his definition) have steep caprock sides. However, our results suggest that the cliff-forming caprocks instead are due to significant erosional backwasting of a once larger channel-belt sandstone body (Fig. 13). Like Utah, Mars ridges also show exposed strata along cliff-forming caprocks and ridges (e.g., Weitz et al., 2008; Wiseman et al., 2008; DiBiase et al., 2013), suggesting significant lateral erosion has occurred, further complicating the interpretation of ridge breadth.

A final implication for Mars is that deposit inversion requires a prolonged surface environment that supported fluvial activity and rivers aggrading, in cases, >300 m of strata (Kite et al., 2013), followed by a transition to regional erosion and exhumation. On Earth deposits of this size form over geologic time (Sadler, 1981) and embedded crater counts of the 300 m of strata in Aeolis Dorsa suggest it formed over at least millions of years (Kite et al., 2013). Other fluvial sinuous ridges across Mars are interpreted to represent fluvial systems ranging in age from mid-Noachian (Davis et al., 2016) to early- and mid-Hesperian (Weitz et al., 2010; Kite et al., 2013), which overlaps with the latest interpretations of fluvial activity indicated by valley networks (Ramirez and Craddock, 2018). Valley networks have been the basis of interpreting fluvial activity on Mars, including location and timing (Hynek et al., 2010) and total volume of water flow (Luo et al., 2017), but debate remains on whether flows occurred sporadically as the result of rare events like impacts (Segura et al., 2002) or were due to a persistent hydrological cycle (Ramirez and Craddock, 2018). Valley networks are erosional fluvial landforms, and erosional systems in general are poor recorders of environmental history over deep time. In contrast, sinuous ridges on Mars may be composed of strata from depositional rivers, which can record a rich history of surface environments over millions of years. Moreover, the recognition of ridges as fluvial deposits will expand geographic coverage of geologic indicators of fluvial activity on the martian surface, which are needed to test global climate models, such as the numerous ridges observed in Arabia Terra (Davis et al.,

2016) that appear inconsistent with the "Icy Highlands" hypothesis (Wordsworth et al., 2013). The transition from Noachian and Hesperian depositional fluvial systems to surface deflation by the wind, as indicated by sinuous ridges, likely coincides with the aridification of Mars (Ramirez and Craddock, 2018), which is also interpreted based on myriad other evidence, including sedimentology (Banham et al., 2018), mineral abundance in global stratigraphy (Ehlmann et al., 2011), and valley network abundance (Di Achille and Hynek, 2010).

8. Conclusions

Sinuous ridges in the Cedar Mountain Formation near Green River, Utah, extend for hundreds of meters, are up to 130 m wide, and stand up to 40 m above the surrounding plain. Ridge caprocks are composed of 3–10 meter-thick sandstone bodies, with dune and bar inclined strata, which we interpret as channel belts that record the lateral migration and aggradation of single-threaded, sand-bedded rivers with 2.1–4.2 m channel depths, rather than channel fills. Some ridges are bisected into segments by washes that preferentially erode portions that are convex in the direction of tectonic dip, and caprocks also degrade laterally by scarp retreat. Due to the combination of amalgamation, erosion, and tectonic modification, ridge dimensions do not record paleo-channel dimensions and ridge top slope is altered to the point that some ridges dip opposite to the inferred paleo-flow direction. From our observations in Utah and a global compilation of terrestrial channel belts, caprock breadth is found to be a potentially unreliable indicator of paleo-channel width because caprocks are eroded remnants of channel-belt sandstone bodies that were once much wider than the paleo-channel, with ridge-to-channel width ratios that could range between 0.2 and 36. In contrast, caprock thickness is more tightly constrained to 0.8–4 times the paleo-channel depth due to the mechanics of river avulsion and channel-belt abandonment, and erosion dominated by scarp retreat. Ridge intersections in planview typically result from crossing of unrelated sandstone bodies at different stratigraphic levels, rather than a bifurcating channel network.

For sinuous ridges formed by exhumation of fluvial channel belts, like in the Cedar Mountain Formation, we developed a method for reconstructing the original channel dimensions and discharge using remote sensing alone for applicability on Mars. The reconstruction is based on measuring the caprock thickness, and using this value to constrain channel depth. Based on our observations in Utah and a compilation of terrestrial channel belts, we caution against using ridge width and curvature as proxies for channel width and curvature; since the ridges are eroded remnants of channel belts, they can have geometries much different than the original channels. An example from Aeolis Dorsa, Mars, shows that mistaking ridge width for channel width could result in significant error in estimated river discharge. More importantly, the ridges on Mars are unlikely to be a snapshot of a paleolandscape, but instead indicate exhumation of a fluvial depositional basin formed over geologic time periods. Such new interpretations would bolster the hypothesis of consistent long-lived fluvial systems on early Mars.

Supplementary data to this article can be found online at https://doi.org/10.1016/j.icarus.2019.04.019.

Acknowledgements

Field data collection was aided by the 2015 field classes of Texas A&M, University of Wyoming, and Caltech. This work was supported by NASA (grant NNX16AQ81G to Caltech and NNX13AG83G to RMEW), Caltech's Terrestrial Hazard Observation and Reporting program, and the Donors of the American Chemical Society Petroleum Research Fund (53544DNI8 to RCE). ATH acknowledges graduate fellowship support from NASA (80NSSC17K0492) and NSF (1144469). We also thank two anonymous reviewers for their helpful comments.

Declaration of interests

None.

References

Anderson, R., Bell, J., 2010. Geologic mapping and characterization of Gale Crater and implications for its potential as a Mars Science Laboratory landing site. Mars J 5, 76–128.
Balme, M.R., Grindrod, P.M., Sefton-Nash, E., Davis, J.M., Gupta, S., Fawdon, P., 2016. Aram dorsum: a noachian inverted fluvial channel system in Arabia Terra, Mars (and candidate ExoMars 2018 rover landing site). In: Lunar and Planetary Science Conference. vol. 47. pp. 2633.
Banham, S.G., et al., 2018. Ancient Martian aeolian processes and palaeomorphology reconstructed from the Stimson formation on the lower slope of Aeolis Mons, Gale crater, Mars. Sedimentology 65 (4), 993–1042.
Bates, C.E., 1952. Photogeologic maps of the stinking Spring Creek 13 and 14 quadrangles, Emery County, Utah. In: Open-File Report.
Best, J.L., Ashworth, P.J., Bristow, C.S., Roden, J., 2003. Three-dimensional sedimentary architecture of a large, mid-channel sand braid bar, Jamuna River, Bangladesh. J. Sediment. Res. 73, 516–530.
Bhattacharya, J.P., Copeland, P., Lawton, T.F., Holbrook, J., 2016. Estimation of source area, river paleo-discharge, paleoslope, and sediment budgets of linked deep-time depositional systems and implications for hydrocarbon potential. Earth Sci. Rev. 153, 77–110.
Blum, M., Martin, J., Milliken, K., Garvin, M., 2013. Paleovalley systems: insights from Quaternary analogs and experiments. Earth Sci. Rev. 116, 128–169.
Bradley, R.W., Venditti, J.G., 2017. Reevaluating dune scaling relations. Earth Sci. Rev. 165, 356–376.
Bridge, J., 2003. Rivers and Floodplains. Blackwell Publishing, Malden, Mass.
Bridge, J.S., Lunt, I.A., 2006. Depositional models of braided rivers. In: Braided Rivers: Process, Deposits, Ecology and Management. 36. pp. 11e50.
Bridge, J., Smith, N., Trent, F., Gabel, S., Bernstein, P., 1986. Sedimentology and morphology of a low-sinuosity river: Calamus River, Nebraska Sand Hills. Sedimentology 33, 851–870.
Bryant, M., Falk, P., Paola, C., 1995. Experimental study of avulsion frequency and rate of deposition. Geology 23, 365–368.
Burr, D.M., Enga, M.-T., Williams, R.M.E., Zimbelman, J.R., Howard, A.D., Brennand, T.A., 2009. Pervasive aqueous paleoflow features in the Aeolis/Zephyria Plana region, Mars. Icarus 200, 52–76.
Burr, D.M., Williams, R.M.E., Wendell, K.D., Chojnacki, M., Emery, J.P., 2010. Inverted fluvial features in the Aeolis/Zephyria Plana region, Mars: formation mechanism and initial paleodischarge estimates. Journal of Geophysical Research: Planets 1991–2012, 115.
Cardenas, B.T., Mohrig, D., Goudge, T.A., 2017. Fluvial stratigraphy of valley fills at Aeolis Dorsa, Mars: evidence for base-level fluctuations controlled by a downstream water body. GSA Bull. 130, 484–498.
Clarke, J.D.A., Stoker, C.R., 2011. Concretions in exhumed and inverted channels near Hanksville Utah: implications for Mars. Int. J. Astrobiol. 10, 161–175.
Cuevas Martínez, J.L., Cabrera Pérez, L., Marcuello, A., Arbués Cazo, P.A.U., Marzo Carpio, M., Bellmunt, F., 2010. Exhumed channel sandstone networks within fluvial fan deposits from the Oligo-Miocene Caspe Formation, South-east Ebro Basin (Northeast Spain). Sedimentology 57, 162–189.
Currie, B.S., 2002. Structural configuration of the early cretaceous cordilleran foreland-basin system and Sevier Thrust Belt, Utah and Colorado. The Journal of Geology 110, 697–718.
Davis, J.M., Balme, M., Grindrod, P.M., Williams, R.M.E., Gupta, S., 2016. Extensive Noachian fluvial systems in Arabia Terra: implications for early Martian climate. Geology 44, 847–850.
DeCelles, P.G., Coogan, J.C., 2006. Regional structure and kinematic history of the Sevier fold-and-thrust belt, central Utah. Geol. Soc. Am. Bull. 118, 841–864.
DeCelles, P.G., Currie, B.S., 1996. Long-term sediment accumulation in the Middle Jurassic–early Eocene Cordilleran retroarc foreland-basin system. Geology 24, 591–594.
Derr, M.E., 1974. Sedimentary Structure and Depositional Environment of Paleochannels in the Jurassic Morrison Formation near Green River, Utah. Brigham Young University, Dept. of Geology.
Di Achille, G., Hynek, B.M., 2010. Ancient ocean on Mars supported by global distribution of deltas and valleys. Nat. Geosci. 3, 459–463.
DiBiase, R.A., Limaye, A.B., Scheingross, J.S., Fischer, W.W., Lamb, M.P., 2013. Deltaic deposits at Aeolis Dorsa: sedimentary evidence for a standing body of water on the northern plains of Mars. Journal of Geophysical Research: Planets 118, 1285–1302.
Doelling, H.H., Kuehne, P.A., Willis, G.C., Ehler, J.B., 2015. Geologic Map of the San Rafael Desert 30'x60' Quadrangle, Emery and Grand Counties, Utah.
Durkin, P.R., Boyd, R.L., Hubbard, S.M., Shultz, A.W., Blum, M.D., 2017. Three-dimensional reconstruction of Meander-Belt evolution, cretaceous McMurray Formation, Alberta Foreland Basin, Canada. J. Sediment. Res. 87, 1075–1099.
Eaton, B., 2013. Hydraulic geometry: Empirical investigations and theoretical approaches. In: Treatise on Geomorphology, Fluvial Geomorphology. 9. pp. 313–329.
Ehlmann, B.L., et al., 2011. Subsurface water and clay mineral formation during the early history of Mars. Nature 479, 53–60.
Einstein, H.A., 1950. The Bed-load Function for Sediment Transportation in Open Channel Flows. Citeseer.
Engelund, F., Hansen, E., 1967. A Monograph on Sediment Transport in Alluvial Streams.

Tekniskforlag Skelbrekgade 4, Copenhagen V, Denmark.
Fassett, C.I., Head, J.W., 2005. Fluvial sedimentary deposits on Mars: ancient deltas in a crater lake in the Nili Fossae region. Geophys. Res. Lett. 32.
Fawdon, P., et al., 2018. The Hypanis Valles delta: the last highstand of a sea on early Mars? Earth Planet. Sci. Lett. 500, 225–241.
Ferguson, R., 2007. Flow resistance equations for gravel-and boulder-bed streams. Water Resour. Res. 43.
Fernandes, A.M., Tornqvist, T.E., Straub, K.M., Mohrig, D., 2016. Connecting the backwater hydraulics of coastal rivers to fluvio-deltaic sedimentology and stratigraphy. Geology 44, 979–982.
Foreman, B.Z., Heller, P.L., Clementz, M.T., 2012. Fluvial response to abrupt global warming at the Palaeocene/Eocene boundary. Nature 491, 92–95.
Friend, P.F., 1989. Space and time analysis of river systems, illustrated by Miocene systems of the northern Ebro Basin in Aragon, Spain. Rev. Soc. Geol. Esp. 2, 55–64.
Friend, P.F., Slater, M.J., Williams, R.C., 1979. Vertical and lateral building of river sandstone bodies, Ebro Basin, Spain. J. Geol. Soc. 136, 39–46.
Ganti, V., Chu, Z., Lamb, M.P., Nittrouer, J.A., Parker, G., 2014a. Testing morphodynamic controls on the location and frequency of river avulsions on fans versus deltas: Huanghe (Yellow River), China. Geophys. Res. Lett. 41, 7882–7890.
Ganti, V., Lamb, M.P., McElroy, B., 2014b. Quantitative bounds on morphodynamics and implications for reading the sedimentary record. Nat. Commun. 5, 3298.
Garcia, M.H., 2006. ASCE manual of practice 110—sedimentation engineering: processes, measurements, modeling and practice. World Environmental and Water Resource Congress 2006: Examining the Confluence of Environmental and Water Concerns 1–4.
Garrison, J.R., Brinkman, D., Nichols, D.J., Layer, P., Burge, D., Thayn, D., 2007. A multidisciplinary study of the Lower Cretaceous Cedar Mountain Formation, Mussentuchit Wash, Utah: a determination of the paleoenvironment and paleoecology of the Eolambia caroljonesa dinosaur quarry. Cretac. Res. 28, 461–494.
Gibling, M.R., 2006. Width and thickness of fluvial channel bodies and valley fills in the geological record: a literature compilation and classification. J. Sediment. Res. 76, 731–770.
Goudge, T.A., Mohrig, D., Cardenas, B.T., Hughes, C.M., Fassett, C.I., 2018. Stratigraphy and paleohydrology of delta channel deposits, Jezero crater, Mars. Icarus 301, 58–75.
Grant, J.A., Wilson, S.A., 2012. A possible synoptic source of water for alluvial fan formation in southern Margaritifer Terra, Mars. Planetary and Space Science 72, 44–52.
Grotzinger, J., Hayes, A., Lamb, M., McLennan, S., 2013. Sedimentary processes on earth, Mars, titan, and Venus. Comparative Climatology of Terrestrial Planets. 1, 439–472.
Hajek, E.A., Heller, P.L., 2012. Flow-depth scaling in alluvial architecture and nonmarine sequence stratigraphy; example from the Castlegate Sandstone, central Utah, U.S.A. J. Sediment. Res. 82, 121–130.
Hajek, E.A., Wolinsky, M.A., 2012. Simplified process modeling of river avulsion and alluvial architecture: connecting models and field data. Sediment. Geol. 257–260, 1–30.
Harris, D.R., 1980. Exhumed Paleochannels in the Lower Cretaceous Cedar Mountain Formation near Green River, Utah. Brigham Young University.
Heller, P.L., Paola, C., 1996. Downstream changes in alluvial architecture: an exploration of controls on channel-stacking patterns. J. Sediment. Res. 66.
Hynek, B.M., Beach, M., Hoke, M.R., 2010. Updated global map of Martian valley networks and implications for climate and hydrologic processes. Journal of Geophysical Research: Planets 115.
Ielpi, A., Ghinassi, M., 2014. Planform architecture, stratigraphic signature and morphodynamics of an exhumed Jurassic meander plain (Scalby Formation, Yorkshire, UK). Sedimentology 61, 1923–1960.
Ielpi, A., Ghinassi, M., 2015. Planview style and palaeodrainage of Torridonian channel belts: Applecross Formation, Stoer Peninsula, Scotland. Sediment. Geol. 325, 1–16.
Irwin, R.P., Lewis, K.W., Howard, A.D., Grant, J.A., 2015. Paleohydrology of Eberswalde crater, Mars. Geomorphology 240, 83–101.
Jacobsen, R.E., Burr, D.M., 2017. Dichotomies in the fluvial and alluvial fan deposits of the Aeolis Dorsa, Mars: implications for weathered sediment and paleoclimate. Geosphere 13, 2154–2168.
Jacobsen, R.E., Burr, D.M., 2018. Errors in Martian paleodischarges skew interpretations of hydrologic history: case study of the Aeolis Dorsa, Mars, with insights from the Quinn River, NV. Icarus 302, 407–417.
Jaumann, R., et al., 2008. Fluvial erosion and post-erosional processes on titan. Icarus 197, 526–538.
Jerolmack, D.J., Mohrig, D., 2007. Conditions for branching in depositional rivers. Geology 35, 463–466.
Jerolmack, D.J., Swenson, J.B., 2007. Scaling relationships and evolution of distributary networks on wave-influenced deltas. Geophys. Res. Lett. 34.
Jerolmack, D.J., Mohrig, D., Zuber, M.T., Byrne, S., 2004. A minimum time for the formation of Holden Northeast fan, Mars. Geophys. Res. Lett. 31.
Jobe, Z.R., Howes, N.C., Auchter, N.C., 2016. Comparing submarine and fluvial channel kinematics: implications for stratigraphic architecture. Geology 44, 931–934.
Kargel, J.S., Strom, R.G., 1992. Ancient glaciation on Mars. Geology 20, 3–7.
Kirk, R., et al., 2008. Ultrahigh resolution topographic mapping of Mars with MRO HiRISE stereo images: meter-scale slopes of candidate Phoenix landing sites. Journal of Geophysical Research: Planets 113.
Kirkland, J.I., et al., 1997. Lower to middle Cretaceous dinosaur faunas of the central Colorado Plateau: a key to understanding 35 million years of tectonics, sedimentology, evolution, and biogeography. Brigham Young University Geology Studies 42, 69–104.
Kirkland, J.I., et al., 1999. Distribution of vertebrate faunas in the Cedar Mountain Formation, east-central Utah. Vertebrate Paleontology in Utah: Utah Geological Survey Miscellaneous Publication 1, 201–217.
Kite, E.S., Lucas, A., Fassett, C.I., 2013. Pacing early Mars river activity: embedded craters in the Aeolis dorsa region imply river activity spanned $\gtrsim(1-20)$ Myr. Icarus 225, 850–855.
Kite, E.S., Howard, A.D., Lucas, A.S., Armstrong, J.C., Aharonson, O., Lamb, M.P., 2015a. Stratigraphy of Aeolis dorsa, Mars: stratigraphic context of the great river deposits. Icarus 253, 223–242.
Kite, E.S., Howard, A.D., Lucas, A., Lewis, K.W., 2015b. Resolving the era of river-forming climates on Mars using stratigraphic logs of river-deposit dimensions. Earth Planet. Sci. Lett. 420, 55–65.
Lamb, M.P., Venditti, J.G., 2016. The grain size gap and abrupt gravel-sand transitions in rivers due to suspension fallout. Geophys. Res. Lett. 43, 3777–3785.
Lamb, M.P., Grotzinger, J.P., Southard, J.B., Tosca, N.J., 2012a. Were aqueous ripples on Mars formed by flowing brines. In: Sedimentary Geology of Mars. 102. pp. 139–150.
Lamb, M.P., Nittrouer, J.A., Mohrig, D., Shaw, J., 2012b. Backwater and river plume controls on scour upstream of river mouths: implications for fluvio-deltaic morphodynamics. Journal of Geophysical Research: Earth Surface 117.
Le Deit, L., Hauber, E., Fueten, F., Pondrelli, M., Rossi, A.P., Jaumann, R., 2013. Sequence of infilling events in Gale Crater, Mars: results from morphology, stratigraphy, and mineralogy. Journal of Geophysical Research: Planets 118, 2439–2473.
Leclair, S.F., Bridge, J.S., 2001. Quantitative interpretation of sedimentary structures formed by river dunes. J. Sediment. Res. 71, 713–716.
Lefort, A., Burr, D.M., Beyer, R.A., Howard, A.D., 2012. Inverted fluvial features in the Aeolis-Zephyria Plana, western Medusae Fossae Formation, Mars: evidence for post-formation modification. Journal of Geophysical Research: Planets 117.
Lefort, A., Burr, D.M., Nimmo, F., Jacobsen, R.E., 2015. Channel slope reversal near the Martian dichotomy boundary: testing tectonic hypotheses. Geomorphology 240, 121–136.
Loizeau, D., et al., 2015. History of the clay-rich unit at Mawrth Vallis, Mars: high-resolution mapping of a candidate landing site. Journal of Geophysical Research: Planets 120, 1820–1846.
Ludvigson, G.A., et al., 2015. The emerging terrestrial record of Aptian-Albian global change. Cretac. Res. 56, 1–24.
Luo, W., Cang, X., Howard, A.D., 2017. New Martian valley network volume estimate consistent with ancient ocean and warm and wet climate. Nat. Commun. 8, 15766.
Lynds, R.M., Mohrig, D., Hajek, E.A., Heller, P.L., 2014. Paleoslope reconstruction in sandy suspended-load-dominant rivers. J. Sediment. Res. 84, 825–836.
Mackey, S.D., Bridge, J.S., 1995. Three-dimensional model of alluvial stratigraphy: theory and application. J. Sediment. Res. 65.
Maizels, J.K., 1987. Plio-Pleistocene raised channel systems of the western Sharqiya (Wahiba), Oman. Geol. Soc. Lond., Spec. Publ. 35, 31–50.
Maizels, J.K., 1990. Raised channel systems as indicators of palaeohydrologic change: a case study from Oman. Palaeogeogr. Palaeoclimatol. Palaeoecol. 76, 241–277.
Malin, M.C., Edgett, K.S., 2003. Evidence for persistent flow and aqueous sedimentation on early Mars. Science 302, 1931–1934.
Martin, J., Fernandes, A.M., Pickering, J., Howes, N., Mann, S., McNeil, K., 2018. The stratigraphically preserved signature of persistent backwater dynamics in a large paleodelta system: the Mungaroo Formation, North West Shelf, Australia. J. Sediment. Res. 88, 850–872.
Matsubara, Y., Howard, A.D., Burr, D.M., Williams, R.M.E., Dietrich, W.E., Moore, J.M., 2015. River meandering on Earth and Mars: a comparative study of Aeolis Dorsa meanders, Mars and possible terrestrial analogs of the Usuktuk River, AK, and the Quinn River, NV. Geomorphology 240, 102–120.
Miall, A.D., 1994. Reconstructing fluvial macroform architecture from two-dimensional outcrops: examples from the Castlegate Sandstone, Book Cliffs. Utah. Journal of Sedimentary Research 64.
Miall, A.D., 1996. The Geology of Fluvial Deposits. Springer.
Milliken, K.T., Blum, M.D., Snedden, J.W., Galloway, W.E., 2018. Application of fluvial scaling relationships to reconstruct drainage-basin evolution and sediment routing for the cretaceous and Paleocene of the Gulf of Mexico. Geosphere 14, 749–767.
Mohrig, D., Heller, P.L., Paola, C., Lyons, W.J., 2000. Interpreting avulsion process from ancient alluvial sequences: Guadalope-Matarranya system (northern Spain) and Wasatch formation (western Colorado). Geol. Soc. Am. Bull. 112, 1787–1803.
Moore, J.M., Howard, A.D., Dietrich, W.E., Schenk, P.M., 2003. Martian layered fluvial deposits: implications for Noachian climate scenarios. Geophys. Res. Lett. 30.
Musial, G., Reynaud, J.-Y., Gingras, M.K., Féniès, H., Labourdette, R., Parize, O., 2012. Subsurface and outcrop characterization of large tidally influenced point bars of the Cretaceous McMurray Formation (Alberta, Canada). Sediment. Geol. 279, 156–172.
Nuse, B.R., 2015. Flow processes and sedimentation in a low-sinuosity high net-sand content fluvial channel belt: 3D outcrop study of the Cedar Mountain Formation, Utah. [MS Thesis]. Arthur Lakes Library, Colorado School of Mines.
Okolo, S.A., 1983. Fluvial distributary channels in the Fletcher Bank Grit (Namurian R2b), at Ramsbottom, Lancashire, England. In: Modern and Ancient Fluvial Systems. International Association of Sedimentologists Special Publication 6, pp. 421–433.
Olsen, H., 1988. The architecture of a sandy braided-meandering river system: an example from the lower triassic Soiling Formation (M. Buntsandstein) in W-Germany. Geol. Rundsch. 77, 797–814.
Osterkamp, W.R., Hedman, E.R., 1982. Perennial-Streamflow Characteristics Related to Channel Geometry and Sediment in Missouri River Basin.
Pain, C.F., Ollier, C.D., 1995. Inversion of relief—a component of landscape evolution. Geomorphology 12, 151–165.
Pain, C.F., Clarke, J.D.A., Thomas, M., 2007. Inversion of relief on Mars. Icarus 190, 478–491.
Palucis, M.C., et al., 2014. The origin and evolution of the Peace Vallis fan system that drains to the Curiosity landing area, Gale Crater, Mars. Journal of Geophysical Research: Planets 119, 705–728.
Paola, C., Borgman, L., 1991. Reconstructing random topography from preserved stratification. Sedimentology 38, 553–565.

Paola, C., Mohrig, D., 1996. Palaeohydraulics revisited: palaeoslope estimation in coarse-grained braided rivers. Basin Res. 8, 243–254.
Parker, G., Wilcock, P.R., Paola, C., Dietrich, W.E., Pitlick, J., 2007. Physical basis for quasi-universal relations describing bankfull hydraulic geometry of single-thread gravel bed rivers. Journal of Geophysical Research: Earth Surface 112.
Ramirez, R.M., Craddock, R.A., 2018. The geological and climatological case for a warmer and wetter early Mars. Nat. Geosci. 11, 230–237.
Reijenstein, H.M., Posamentier, H.W., Bhattacharya, J.P., 2011. Seismic geomorphology and high-resolution seismic stratigraphy of inner-shelf fluvial, estuarine, deltaic, and marine sequences, Gulf of Thailand. AAPG Bull. 95, 1959–1990.
Robinson, J.W., McCabe, P.J., 1997. Sandstone-body and shale-body dimensions in a braided fluvial system: Salt Wash Sandstone Member (Morrison Formation), Garfield County, Utah. AAPG Bull. 81, 1267–1291.
Sable, V.H., 1958. Photogeologic map of the Tidwell-2 quadrangle, Emergy and grand counties, Utah. In: Miscellaneous Geologic Investigations. USGS (pp. Map I-162).
Sadler, P.M., 1981. Sediment accumulation rates and the completeness of stratigraphic sections. The Journal of Geology 569–584.
Schumm, S.A., 1972. Fluvial paleochannels. In: Special Publication - Society of Economic Paleontologists and Mineralogists.
Segura, T.L., Toon, O.B., Colaprete, A., Zahnle, K., 2002. Environmental effects of large impacts on Mars. Science. 298, 1977–1980.
Slingerland, R., Smith, N.D., 2004. River avulsions and their deposits. Annu. Rev. Earth Planet. Sci. 32, 257–285.
Southard, J.B., Boguchwal, L.A., 1990. Bed configurations in steady unidirectional water flows; part 3, effects of temperature and gravity. J. Sediment. Res. 60, 680–686.
Stokes, W.L., 1944. Morrison Formation and related deposits in and adjacent to the Colorado Plateau. Geol. Soc. Am. Bull. 55, 951–992.
Stokes, W.L., 1953. Primary Sedimentary Trend Indicators as Applied to Ore Finding in the Carrizo Mountains, Arizona and New Mexico; Part 1, Technical Report for April 1, 1952 to March 31, 1953. U. S. Atomic Energy Commission, Washington, DC, United States, United States.
Stokes, W.L., 1961. Fluvial and eolian sandstone bodies in Colorado Plateau. In: American Association of Petroleum Geologists Special Volume.
Trampush, S.M., Huzurbazar, S., McElroy, B.J., 2014. Empirical assessment of theory for bankfull characteristics of alluvial channels. Water Resour. Res. 50, 9211–9220.
Wang, J., Bhattacharya, J.P., 2018. Plan-view paleochannel reconstruction of amalgamated meander belts, Cretaceous Ferron Sandstone, Notom Delta, South-central Utah, USA. J. Sediment. Res. 88, 58–74.
Ward, D.J., Berlin, M.M., Anderson, R.S., 2011. Sediment dynamics below retreating cliffs. Earth Surf. Process. Landf. 36, 1023–1043.
Weitz, C.M., Milliken, R., Grant, J.A., McEwen, A.S., Williams, R.M.E., Bishop, J.L., 2008. Light-toned strata and inverted channels adjacent to Juventae and Ganges chasmata, Mars. Geophys. Res. Lett. 35.
Weitz, C.M., et al., 2010. Mars Reconnaissance Orbiter observations of light-toned layered deposits and associated fluvial landforms on the plateaus adjacent to Valles Marineris. Icarus 205, 73–102.
Wilkerson, G.V., Parker, G., 2011. Physical basis for quasi-universal relationships describing bankfull hydraulic geometry of sand-bed rivers. J. Hydraul. Eng. 137, 739–753.
Williams, G.P., 1984. Paleohydrologic equations for rivers. In: Developments and Applications of Geomorphology. Springer, pp. 343–367.
Williams, G.P., 1988. Paleofluvial estimates from dimensions of former channels and meanders. In: Flood Geomorphology. 1988. John Wiley & Sons, New York, pp. 321–334.
Williams, R.M.E., 2007. Global spatial distribution of raised curvilinear features on Mars. In: Lunar and Planetary Science Conference. Vol. 38. pp. 1821.
Williams, R.M.E., Weitz, C.M., 2014. Reconstructing the aqueous history within the southwestern Melas basin, Mars: clues from stratigraphic and morphometric analyses of fans. Icarus 242, 19–37.
Williams, R.M.E., Chidsey Jr., T.C., Eby, D.E., 2007. Exhumed Paleochannels in Central Utah—Analogs for Raised Curvilinear Features on Mars. Diverse Geology of a Dynamic Landscape, Central Utah, pp. 221–235.
Williams, R.M.E., Irwin, R.P., Zimbelman, J.R., 2009. Evaluation of paleohydrologic models for terrestrial inverted channels: implications for application to martian sinuous ridges. Geomorphology 107, 300–315.
Williams, R.M.E., Irwin, R.P., Zimbelman, J.R., Chidsey, T.C., Eby, D.E., 2011. Field guide to exhumed paleochannels near Green River, Utah: terrestrial analogs for sinuous ridges on Mars. Geol. Soc. Am. Spec. Pap. 483, 483–505.
Williams, R.M.E., Irwin, R.P., Burr, D.M., Harrison, T., McClelland, P., 2013. Variability in martian sinuous ridge form: case study of Aeolis Serpens in the Aeolis dorsa, Mars, and insight from the Mirackina paleoriver, South Australia. Icarus 225, 308–324.
Wiseman, S.M., et al., 2008. Phyllosilicate and sulfate-hematite deposits within Miyamoto crater in southern Sinus Meridiani, Mars. Geophys. Res. Lett. 35.
Witkind, I.J., 1988. Geologic map of the Huntington 30'x60' Quadrangle, Carbon, Emery, Grand, and Uintah Counties, Utah.
Wordsworth, R., Forget, F., Millour, E., Head, J.W., Madeleine, J.B., Charnay, B., 2013. Global modelling of the early martian climate under a denser CO2 atmosphere: water cycle and ice evolution. Icarus 222, 1–19.
Wu, C., Ullah, M.S., Lu, J., Bhattacharya, J.P., 2016. Formation of point bars through rising and falling flood stages: evidence from bar morphology, sediment transport and bed shear stress. Sedimentology 63 (6), 1458–1473.
Zaki, A.S., Pain, C.F., Edgett, K.S., Giegengack, R., 2018. Inverted stream channels in the Western Desert of Egypt: synergistic remote, field observations and laboratory analysis on Earth with applications to Mars. Icarus 309, 105–124.
Zaleha, M.J., 2013. Paleochannel hydraulics, geometries, and associated alluvial architecture of Early Cretaceous rivers, Sevier Foreland Basin, Wyoming, USA. Cretac. Res. 45, 321–341.
Zimbelman, J.R., Griffin, L.J., 2010. HiRISE images of yardangs and sinuous ridges in the lower member of the Medusae Fossae Formation, Mars. Icarus 205, 198–210.